Pharmacologic hyperstabilisation of the HIV-1 capsid lattice induces capsid failure

K. M. Rifat Faysal[1,#], James Walsh[1,#], Nadine Renner[2,‡], Chantal L. Márquez[1,‡], Vaibhav B. Shah[1], Andrew J. Tuckwell[1], Michelle P. Christie[3], Michael W. Parker[3,4], Stuart G. Turville[5], Greg J. Towers[6], Leo James[2], David A. Jacques[1,*], Till Böcking[1,*]

1. EMBL Australia Node in Single Molecule Science, School of Biomedical Sciences, UNSW Sydney, NSW 2052, Australia

2. MRC Laboratory of Molecular Biology, Cambridge, United Kingdom

3. Department of Biochemistry and Pharmacology, Bio21 Molecular Science and Biotechnology Institute, University of Melbourne, Victoria 3010, Australia

4. Structural Biology Unit, St. Vincent's Institute of Medical Research, Victoria, Australia

5. The Kirby Institute, UNSW Sydney, NSW 2052, Australia

6. Division of Infection and Immunity, University College London, WC1E 6BT London, United Kingdom

[#]equal contribution
[‡]equal contribution
*Corresponding authors: David Jacques (d.jacques@unsw.edu.au); Till Böcking (till.boecking@unsw.edu.au)

Abstract

The HIV-1 capsid has emerged as a tractable target for antiretroviral therapy. Lenacapavir, developed by Gilead Sciences, is the first capsid-targeting drug approved for medical use. Here we investigate the effect of Lenacapavir on HIV capsid stability and uncoating. We employ a single particle approach that simultaneously measures capsid content release and lattice persistence. We demonstrate that Lenacapavir's potent antiviral activity is predominantly due to lethal hyperstabilisation of the capsid lattice and resultant loss of compartmentalisation. This study highlights that disrupting capsid metastability is a powerful strategy for the development of novel antivirals.

Introduction

The cell is a hostile environment for HIV, as the reverse transcribed cDNA genome is a target for innate immune sensors which unleash a potent interferon response that can suppress replication (Alvarez et al., 2022; Lahaye et al., 2013; Rasaiyaah et al., 2013). For a productive infection to occur, the reverse transcribing genome must be trafficked through the cytoplasm, enter the nucleus and integrate into the preferred sites in the host chromatin, all while evading detection by the host cell. The viral capsid facilitates these early steps in the replication cycle by encapsulating the genome and associated viral enzymes. In doing so it protects the genome from being sensed and destroyed by nucleases, prevents loss of viral enzymes from the reverse transcription complex, and forms the interface through which all cytoplasmic, and many nuclear, host-virus interactions occur.

The conical capsid shell is comprised of ~1500 copies of the capsid protein (CA), which spontaneously assemble into a lattice. This lattice consists of mostly hexamers and exactly 12 pentamers to form a closed fullerene cone (Ganser et al., 1999; Pornillos et al., 2011). While the capsid must be stable enough to transit the cytoplasmic compartment without exposing the genome, it must also be able to release the reverse transcribed cDNA at the appropriate time and in the appropriate location in the nucleus. This process is called capsid uncoating and its regulation and mechanism are poorly understood. Recently, we demonstrated that uncoating proceeds through two discrete steps *in vitro*: capsids opening, in which the integrity of the cone is compromised and encapsidated proteins are released; and catastrophic disassembly of the lattice by release of CA (Márquez et al., 2018). We have also shown that recruitment of cellular cofactors or binding of pharmacological agents to the capsid can greatly alter both processes.

To engage with host cofactors, the mature HIV capsid utilises at least three cytoplasm-facing surfaces (Temple et al., 2020). One of these is the central pore, which is formed by a ring of positively charged arginine residues at the six-fold symmetry axis in CA hexamers and at the five-fold axis in pentamers (Jacques et al., 2016). It serves to recruit nucleotides required for reverse transcription and as a binding site for inositol hexakisphosphate (IP6), a metabolite present at concentrations of ~40–50 μM in human cells (Bunce et al., 1993; Letcher et al., 2008; Veiga et al., 2006). IP6 is specifically packaged into immature virions during assembly in producer cells, leading to a ≥10–fold enrichment, and its interaction with the central pore is essential for the assembly and stability of the capsid (Dick et al., 2018; Mallery et al., 2018; Obr et al., 2021; Sowd and Aiken, 2021). The central pore has also been implicated in the capsid's interaction with microtubule-based motor proteins (Huang et al., 2019).

Another important interface is the cyclophilin binding loop. As its name suggests, this largely unstructured loop protrudes from the capsid surface to recruit cyclophilin A (CypA). This interaction is mediated by a conserved glycine-proline motif (G89-P90) that inserts into the CypA active site. The implications of this interaction are still to be fully understood, but are thought to include viral evasion of innate host defences (Kim et al., 2019; Miles et al., 2020; Rasaiyaah et al., 2013; Towers et al., 2003). Importantly, we have previously shown that this interaction can be exploited *in vitro* to ‘paint’ the capsid (Márquez et al., 2018). By using a fluorescently labelled CypA, we found that it is possible to detect, quantify, and monitor disassembly of the CA lattice in permeabilised virions by total internal reflection fluorescence (TIRF) microscopy without significantly influencing the capsid opening process.

The third host-interaction surface, the FG-binding site, is a hydrophobic pocket in the CA N-terminal domain situated near the intra-hexameric junction between CA molecules (Figure 1). This site serves as the binding interface for several host factors, including the cytoplasmic protein Sec24C (Rebensburg et al., 2021), components of the nuclear pore complex including NUP153 (Matreyek et al., 2013) and other permeability barrier-forming nucleoporins (Dickson et al., 2023), and the nuclear protein CPSF6 (Bhattacharya et al., 2014; Price et al., 2014). Sequential interactions with these proteins are crucial for nuclear entry and correct integration site targeting (Bejarano et al., 2019; Saito et al., 2016; Schaller et al., 2011). Each of these proteins interacts with the capsid via a phenylalanine-glycine (FG) motif. Additionally, several generations of antiviral compounds also target this site by effectively mimicking the FG-motif (Price et al., 2014). Interestingly, the potency and mechanism of action of these agents varies, despite their shared binding site.

Compounds that target the FG-binding pocket include BI-2 (Lamorte et al., 2013), PF74 (Blair et al., 2010), and lenacapavir (LEN, GS-6207) (Link et al., 2020). BI-2 has a relatively small binding footprint on the CA N-terminal domain, barely extending beyond the FG-binding pocket (Figure 1A). This limited interaction is reflected in the relatively weak binding affinity (K_D = 1.2 μM) and high drug concentration required to inhibit infection by 50% during the early stage of infection (half maximal inhibitory concentration, IC50 = 3 μM) (Price et al., 2014). PF74, on the other hand, extends its interaction beyond the FG-binding pocket to make additional contacts with a neighbouring CA molecule (Figure 1B). These bridging contacts are thought to be responsible for PF74's 10-fold tighter K_D (120 nM) and IC50 (relative to BI-2). Both BI-2 and PF74 can compete with host cofactor binding (Sec24C, Nup153, and CPSF6) (Fricke et al., 2014; Matreyek et al., 2013; Peng et al., 2014; Price et al., 2014; Rebensburg et al., 2021), and also directly affect capsid structure and stability. While both compounds have capsid-opening activity (Bhattacharya et al., 2014; Fricke et al., 2014; Shi et al., 2011), leading to a block of reverse transcription (Jennings et al., 2020; Mallery et al., 2018; Sowd et al., 2021), PF74 also increases the stiffness of the capsid (Rankovic et al., 2018) and stabilises hexameric CA lattices (Bhattacharya et al., 2014; Mallery et al., 2018)

In contrast to BI-2 and PF74, which have found use exclusively in the laboratory, LEN is a first-in-class HIV-1 capsid inhibitor in clinical trials and approved by the European Union and by the U.S. Food and Drug Administration for clinical use in patients with multidrug-resistant HIV-1 infection (Dvory-Sobol et al., 2022; Patel et al., 2023). Structurally, LEN makes extensive contacts across two neighbouring CA monomers (Figure 1C), allowing for a very high-affinity interaction (K_D = 215 pM). It interferes with early and late phases of the HIV-1 replication cycle at low and high pM concentrations, respectively, making it orders of magnitude more potent than PF74 and BI-2 (Bester et al., 2020; Link et al., 2020). Successive post-entry steps differ in their sensitivity to the drug (Bester et al., 2020; Link et al., 2020), whereby integration of HIV-1 DNA into host chromatin is inhibited most potently (<500 pM), followed by nuclear import and reverse transcription, which is inhibited at high pM (Sowd et al., 2021) to low nM LEN (Bester et al., 2020). Remarkably, imaging studies (Bester et al., 2020) and biochemical assays (Selyutina et al., 2022) showed that LEN increased the number of viral cores in the cytoplasm in a dose-dependent manner. Thus, the drug exhibited apparently contrasting inhibitory effects at higher concentrations: inhibition of reverse transcription and stabilization of viral cores.

Here we have used single-molecule fluorescence imaging to show that LEN breaks IP6-stabilised capsids while preventing disassembly of CA lattices with open edges. Indirect

visualisation of LEN binding to authentic capsids in real time reveals that capsid breakage depends on the occupancy of FG binding pockets. In vitro assembly assays show that LEN and IP6 synergise to accelerate CA assembly but promote tubular (LEN) versus conical (IP6) structures, leading to the formation aberrant CA structures. Altogether, our data suggest that substoichiometric binding of LEN stabilises the hexameric CA lattice at the cost of fully closed capsids, leading to loss of reverse transcription. This mechanism becomes dominant in the high pM range, close to the inhibitory concentration that leads to 95% inhibition (IC95) of viral replication.

147 # Results
148
149 **Single-virion analysis of intrinsic capsid stability and uncoating.**
150 We used a single-molecule fluorescence imaging assay to measure the intrinsic capsid
151 stability and uncoating kinetics at the level of individual viral particles (Márquez et al., 2018)
152 and then measured the effect of LEN treatment on these processes. As shown schematically
153 in Figure 2A, we used pore-forming proteins to permeabilise GFP-loaded HIV particles
154 immobilised at the bottom surface of a microfluidic channel device. Using TIRF microscopy,
155 we then detected the stepwise loss of the GFP signal for each virion appearing as a bright
156 diffraction-limited spot in the field of view. Upon membrane permeabilization, virions with a
157 "leaky" capsid lost their entire GFP signal in a single step (Figure 2B). In contrast, virions
158 containing an intact capsid retained the pool of GFP inside the capsid. This residual (low
159 intensity) GFP signal was lost in a second step upon spontaneous loss of capsid integrity
160 (Figure 2B, "opening"), whereby the lifetime of each opening capsid was given by the time
161 difference between the two GFP release steps. A subset of GFP-containing capsids remained
162 at the end of the experiment (Figure 2B, "closed"), because the 30-minute imaging period
163 was not long enough to observe opening of all capsids. Finally, virus preparations also
164 contained a subset of immature particles that remain at the initial high intensity level
165 throughout the imaging period because the GFP remains bound to the viral membrane as part
166 of the immature Gag lattice (Figure 2–Figure Supplement 1).
167
168 We used step-fitting to classify the typically 300–1000 virions per field of view according to
169 the GFP release profiles defined above. Immature virions (6.9±3.1% of all particles) were
170 excluded from further analysis. Most of the mature virions showed leaky release profiles
171 (56±5%), which we attribute to incompletely assembled capsids that are also seen in
172 cryoelectron tomography reconstructions of mature HIV (Mattei et al., 2016). Capsids with
173 opening and closed intensity profiles (33.7 ±5.0% and 10.4±3.5%, respectively) were further
174 analysed to quantify the kinetics of capsid opening. We obtained a capsid survival curve
175 (lifetime distribution) by plotting the fraction of capsids that remain intact (GFP-positive) as
176 a function of time. The survival curve for untreated virions (Figure 2D, no drug) showed a
177 biphasic decay profile with ~30% short-lived (half-life of 1.0±0.5 min) and ~70% long-lived
178 (half-life of 15±3 min) capsids, consistent with previous observations (Mallery et al., 2021;
179 Márquez et al., 2018; Renner et al., 2023). Long-lived capsids can be stabilised by the host
180 cofactor IP6 (see below) and are considered functionally relevant (see Figure 2–Figure
181 Supplement 2 for a detailed discussion of the capsid stability types observed in this assay).
182 Control experiment showed that fraction of IP6-stabilised capsids was independent of the
183 concentration of the pore-forming protein used to permeabilise the viral membrane,
184 confirming that it does not affect capsid stability (Figure 2–Figure Supplement 3).
185
186 As a complementary measurement, we used AF568-labelled CypA as a "paint" that binds
187 transiently to the outside of the capsid, rapidly reaching a dynamic equilibrium, whereby the
188 AF568-CypA intensity is proportional to the number of CA subunits in the lattice.
189 Importantly, AF568-CypA was used at concentrations (0.5–1 μM) where fewer than 4% of
190 the available cyclophilin loops are occupied, and we have previously shown that uncoating
191 kinetics are not affected under these conditions (Márquez et al., 2018). Single-particle
192 analysis showed that the AF568-CypA signal remained constant while the capsid was intact
193 (Figure 2B, "closed") but decayed to background levels after the capsid opened (Figure 2B,
194 "leaky" and "opening"). Analysis of all leaky and opening traces aligned to the time of capsid
195 opening showed that the median CypA signal decayed with a half-life of less than 1 minute
196 (Figure 2E). This rapid decay is consistent with a failure cascade that propagates across the

197 whole capsid resulting in complete lattice disassembly. Taken together, our single-particle
198 analysis shows that GFP release pinpoints the time the first defect appears in the capsid while
199 the CypA paint signal provides an indirect read-out for the disassembly kinetics of the CA
200 lattice thereafter.
201
202 **LEN induces capsid opening but prevents loss of CA from the lattice of open capsids.**
203 In the next set of experiments, we focused on the effect of LEN on the intrinsic capsid
204 stability without capsid-binding cofactors; the interplay between LEN and IP6, which is
205 essential for maintaining capsid stability in cells, is described in later sections. To measure
206 the maximum effect of LEN on capsid uncoating, we added the drug at a concentration (500
207 nM) that leads to rapid binding to essentially all FG binding sites. Uncoating traces of single
208 virions in the presence of 500 nM LEN (Figure 2C) revealed two fundamental differences to
209 the single-particle profiles described above. First, LEN treatment caused earlier release of the
210 encapsidated GFP (Figure 2C, "opening"), resulting in a faster decaying survival curve
211 (Figure 2D, light green line) and a concomitant 3-fold decrease in the fraction of closed
212 capsids at the end of the experiment. Second, the AF568-CypA signal of capsids that were
213 defective to begin with (Figure 2C, "leaky") or started to uncoat (Figure 2C, "opening")
214 remained constant. This striking stabilisation effect was also clear in the heatmaps of leaky
215 and opening capsids (Figure 2F, 500 nM LEN). Since the CypA paint traces of leaky and
216 opening capsids showed the same characteristics, we combined these classes in subsequent
217 analyses to assess the extent to which LEN could stabilise the lattice of open capsids. Taken
218 together, the GFP release and CypA paint analysis in the presence of 500 nM LEN suggest
219 that binding of LEN induces rupture of capsids (leading to early GFP release) but prevents
220 the loss of CA subunits from defective or ruptured capsids (stable CypA paint signal).
221
222 To further quantify these apparently opposing effects on capsid integrity and CA lattice
223 stability, we measured GFP release and CypA paint traces in the presence of LEN at
224 concentrations ranging from 5–500 nM (Figure 3). The survival curves (Figure 3A) showed a
225 pronounced concentration-dependent acceleration of capsid opening kinetics with an
226 intermediate effect at 5 nM and the maximal effect at ≥50 nM LEN, leading to a two- to four-
227 fold (5 nM and ≥50 nM LEN, respectively) decrease in the fraction of capsids that remained
228 closed after 15 minutes (Figure 3C). Similarly, we observed a concentration-dependent
229 increase in the fraction of particles with leaky capsids from 56±5% (no drug) to 65±7% (500
230 nM) (Figure 3–Figure Supplement 3), which we attribute to rapid drug-induced capsid
231 rupture that occurred before membrane permeabilization.
232
233 Next, we analysed the CypA paint signal to determine the effect of LEN on the lattice after
234 capsid integrity loss. LEN concentrations of ≥50 nM prevented disassembly of leaky and
235 opening capsids, as evidenced by the stable CypA paint signal (Figure 3C), which persisted
236 for at least 5 h (Figure 3D). Under the conditions used in the single-particle uncoating assay,
237 the capsid is exposed to the membrane-permeable drug for ~2 minutes before the pore
238 forming protein permeabilises the viral membrane. Thus, we first calculated the occupancy at
239 this time point to estimate the threshold required to prevent disassembly of defective capsids
240 (see Methods). Unsurprisingly, the low occupancy at 5 nM LEN (calculated to be <10%) was
241 insufficient for lattice stabilisation. In contrast, 32–66% occupancy at 50 nM LEN, was
242 sufficient to prevent CA lattice disassembly. Based on these considerations, we estimate that
243 2–4 LEN molecules per hexamer are sufficient to prevent the release of CA subunits from a
244 CA lattice with open edges.
245

246 In summary, LEN dose-dependently increased the proportion of open capsids but increased
247 the stability of their lattices. The dose-dependence observed here differs from previous in
248 vitro uncoating measurements showing (partial) capsid lattice stabilisation down to 0.05 nM
249 LEN; in those experiments 50–65% of cores stained with the irreversibly bound tetrameric
250 probe CypA-dsRed remained detectable after 30 min of incubation (Bester et al., 2020).
251 Nevertheless, our observation of capsids that do not lose CA despite having openings is
252 consistent with the LEN dose-dependent increase in the number of CA-positive spots
253 detected in the cytoplasm of infected cells (Bester et al., 2020; Selyutina et al., 2022).
254
255 **IP6 counteracts but does not prevent LEN-induced capsid rupture.**
256 We have previously shown that the cellular cofactor IP6 stabilises capsids and delays capsid
257 opening *in vitro* (Mallery et al., 2018). Since IP6 is present in cells (typically 40–50 μM
258 (Bunce et al., 1993; Letcher et al., 2008)) and therefore expected to impact the effects of LEN
259 *in vivo,* we asked if IP6 could prevent LEN-induced rupture of the capsid. As before, IP6
260 (100 μM) strongly stabilised capsids in permeabilised virions, leading to reduced capsid
261 opening kinetics (Figure 3B) and a ~2-fold increase in the fraction of closed capsids at 15
262 minutes compared to the control without IP6 (Figure 3C). IP6 partially counteracted the
263 capsid-breaking effect at 5 nM LEN (compare Figure 3A and 3B), but even at this
264 concentration the drug increased capsid opening kinetics relative to IP6 only (Figure 3B). At
265 high LEN concentrations (≥50 nM), the survival curves measured in the presence and
266 absence of IP6 were essentially the same, showing that IP6 was no longer able to slow the
267 premature rupture of the capsid induced by the drug (Figure 3B). This acceleration in capsid
268 opening led to an eight-fold reduction in the fraction of closed capsids at 15 min compared to
269 the control with IP6 only (Figure 3B). We conclude that IP6 partially protects capsids from
270 LEN-induced structural damage, but only at low drug concentrations. The higher
271 susceptibility to structural damage in the absence of IP6 is consistent with the observation
272 that LEN more potently inhibits reverse transcription *in vitro* and in cells when IP6 levels are
273 low (Sowd et al., 2021).
274
275 Finally, we asked if IP6 could act in conjunction with LEN to stabilise the CA lattice after
276 capsid opening. As observed for other polyanions binding at the R18 ring at the centre of the
277 CA hexamer (Márquez et al., 2018), IP6 by itself slows but does not prevent the catastrophic
278 collapse of CA lattices with open edges (Figure 3–Figure Supplement 1). CA lattice
279 dissociation of leaky and opening capsids is further slowed when IP6 is added to 5 nM LEN
280 (<10% occupancy of FG sites at the time of membrane permeabilization) (Figure 3–Figure
281 Supplement 2A and B). At 50 nM LEN (>30% occupancy of FG sites), the CypA paint signal
282 remains constant in the presence and absence of IP6 (Figure 3–Figure Supplement 2C and D),
283 such that differences in stability during the time frame of the experiment are difficult to
284 ascertain. Overall, these data suggest that IP6 further stabilises LEN-stabilised CA lattices but
285 not to the extent where it can prevent CA release from lattices at low LEN occupancy.
286
287 **Slow LEN binding kinetics delay the structural drug effects at low concentrations.**
288 Next, we considered the kinetics of LEN binding to explain the observed differences in drug-
289 induced capsid rupture between 5 nM and higher concentrations (50 and 500 nM). The LEN
290 binding curves calculated using published association and dissociation rate constants (Figure
291 4–Figure Supplement 1A) predict that LEN occupancies ≥95% are reached within <2 minutes
292 at 500 nM and ~15 minutes at 50 nM but reaching this level requires almost 3 hours at 5 nM
293 LEN. Thus, we postulated that the intermediate capsid breakage kinetics observed at 5 nM
294 LEN is due to slow binding kinetics such that occupancy levels required for fast capsid
295 breakage are not reached quickly enough within the imaging period. To test this, we

296 preincubated virions with 5 nM LEN for 4 h, during which 95% of sites are occupied.
297 Analysis of GFP release traces showed that preincubation with 5 nM LEN increased the
298 extent of drug-induced capture rupture to that observed at 500 nM without preincubation
299 (Figure 4–Figure Supplement 1B). Notably, >50% of the capsids had apparently already been
300 ruptured inside the viral membrane, leading to an increase in "leaky" traces relative to control
301 (Figure 4–Figure Supplement 1B). This suggests that drug-induced capsid rupture manifests
302 over time and that rupture, or build-up of the strain required for rupture, can already occur
303 before release of the capsid from the virion. Finally, CypA paint analysis showed that CA
304 lattice disassembly was inhibited with, but not without, preincubation (Figure 4–Figure
305 Supplement 1C). Taken together, these observations suggest that the full extent of the capsid-
306 altering effects is observed after binding occupancy reaches the requisite level.
307
308 **Indirect fluorescence imaging of LEN binding kinetics to HIV capsids via displacement**
309 **of a "paint" probe for the FG pocket**
310 To corroborate the LEN binding kinetics, we developed a new imaging assay to measure
311 LEN binding to authentic capsids in real time by displacement of a fluorescent peptide
312 derived from CPSF6 as a "paint" probe that binds dynamically to the FG binding pocket,
313 whereby the binding level is proportional to the fraction of sites that remain unoccupied with
314 the tightly binding drug molecule. The requirement for a paint probe in this assay is that it has
315 fast binding and dissociation kinetics such that it rapidly reaches a dynamic binding
316 equilibrium to probe free sites without blocking them for drug binding. A CPSF6 peptide
317 labelled with a fluorescent dye (CPSF6p, residues 313-327 with a C-terminal cysteine for
318 labelling) fulfilled these criteria, binding with a half-life of 11 s to the capsids of
319 permeabilised virions on the TIRF microscope coverslip (Figure 4–Figure Supplement 2).
320 Using single-molecule photobleaching for calibration of the fluorescence intensity, we
321 determined the number of CPSF6p bound at equilibrium per capsid at a range of
322 concentrations (Figure 4–Figure Supplement 2D). At the CPSF6p paint probe concentration
323 (200 nM) used in the LEN binding assay, ~40 CPSF6p are bound at equilibrium per capsid,
324 occupying <3% of FG binding pockets.
325
326 The design of the LEN binding assay is shown in Figure 4A. GFP-loaded HIV on the
327 coverslip surface were permeabilised using a pore-forming protein and incubated for 2 h in
328 the presence of IP6 (30 μM) and labelled CPSF6p. During this period all capsids that cannot
329 be stabilised by IP6 (leaky and short-lived) decayed away such that only long-lived IP6-
330 stabilised capsids remained. These were identified as spots positive for GFP (as a capsid
331 integrity marker) and CPSF6. We then added LEN to the flow channel and tracked the GFP
332 and CPSF6 signals at the location of individual virions over time. LEN led to a concentration-
333 dependent decay of the CPSF6 intensity (Figure 4B) as LEN increasingly (and irreversibly on
334 the time scale of this experiment) occupies FG binding pockets on the lattice. (We note that
335 photobleaching does not contribute to the signal decay because the bound paint probes
336 continually exchange with fresh molecules from solution). Thus, the decrease in CPSF6
337 intensity is an indirect read-out for LEN binding, and we converted this data into kinetic
338 curves of LEN binding to authentic HIV capsids (Figure 4C). An independent repeat of this
339 set of experiments is shown in Figure 4–Figure Supplement 3A and B. The association rate
340 constant determined from the pooled data of both experiments (k_{on} = 1.84±0.78 × 10^5 M^{-1} s^{-1},
341 Figure 4D) was within a factor of three of the published value (k_{on} = 6.5±0.3 × 10^4 M^{-1} s^{-1}),
342 while the K_D of 0.51±0.58 nM was about two times the published value (K_D = 0.24±0.09 nM)
343 (Link et al., 2020). These differences are within experimental error of our method but could
344 also reflect a difference in binding to an authentic capsid versus binding to a cross-linked CA
345 hexamer used in the published work.

346
347 **LEN-induced capsid rupture kinetics depend on the occupancy of FG binding pockets**
348 Next, we analysed the GFP release traces collected in the LEN-binding TIRF experiments
349 described above (Figure 4A) to extract the capsid opening kinetics (Figure 4F and G).
350 Importantly, the new assay design allows the functionally irrelevant subset of defective/IP6-
351 insensitive capsids to disassemble before measuring the effect of LEN exclusively on the
352 functionally relevant subset of IP6-stabilised capsids. This avoids the complexity of
353 convolving intrinsic instability with drug-induced breakage. Remarkably, the stability of the
354 IP6-responsive capsids in the absence of drug exceeded the level of IP6-mediated
355 stabilisation we have previously observed, and we observed little or no loss of capsids over
356 the 90-minute imaging period (Figure 4F, 0 nM LEN). The same observation held when
357 imaging was extended to 8 h, and we estimate the half-life of IP6-stabilised capsids in this
358 assay design to be on the order of day(s).
359
360 Survival analysis in the presence of 0.2–20 nM LEN (Figure 4F) revealed the following drug
361 effects on capsid stability. Firstly, rupture of IP6-stabilised capsids accelerated with
362 increasing LEN concentrations. This is apparent from the concentration-dependent faster
363 decay of the survival curves and the corresponding decrease of the half-life of the intact
364 capsid (Figure 4G, note the log-log scale) from 4.5 hours at 0.2 nM to 1 hour at 1 nM, with
365 rupture becoming essentially immediate at >20 nM LEN (half-life of 2–3 minutes). Secondly,
366 the survival curves are not purely exponential and show a lag period, especially at the lower
367 end of the concentration range (discussed below). Thirdly, the overall efficiency of capsid
368 rupture decreased sharply toward the lower end of the concentration range, dropping below
369 65% at 0.4 nM LEN (Figure 4–Figure Supplement 3D). We propose that the complex kinetics
370 of LEN-induced capsid failure observed in our experiments are a convolution of (1) LEN
371 concentration-dependent binding kinetics to gradually increase the occupancy of FG binding
372 pockets with LEN and (2) occupancy-dependent kinetics of capsid rupture where higher
373 occupancy leads to the capsid becoming more unstable. It is also likely that capsids have
374 heterogeneous susceptibility to LEN-induced structural damage, reflecting the heterogeneity
375 of capsid architectures. This is supported by the decrease in breakage efficiency with LEN
376 concentration (Figure 4–Figure Supplement 3D).
377
378 The power of using our combined CPSF6 paint and GFP release TIRF assay is that we can
379 measure the LEN occupancy at the time of capsid opening and thus directly relate occupancy
380 to drug-induced structural damage (Figure 4H). Interestingly, the mean LEN occupancy at the
381 time of capsid rupture increased with LEN concentration. At sub-nM concentrations, LEN
382 induced breakage when 20–30% of FG sites were drug-bound. At LEN concentrations ≥10
383 nM, the mean occupancy at the time of capsid breakage levelled off at ~70%. Taken together,
384 our data suggest that LEN-induced capsid breakage can occur at low occupancies, albeit
385 slowly. Breakage typically occurs at higher occupancies when LEN binding kinetics outpace
386 the (occupancy-dependent) breakage kinetics. At high LEN occupancy (above 70%), capsids
387 become so overwhelmingly unstable that it is practically impossible to bind LEN fast enough
388 to get to complete occupancy before the capsid ruptures.
389
390 In summary, we conclude that efficient and rapid capsid breakage depends on reaching a
391 sufficient occupancy of FG binding pockets, which itself depends on binding kinetics if drugs
392 are added at the beginning of the experiment. At the lowest concentrations tested here (0.2
393 nM) LEN can break capsids, but slowly and only for a subset of capsids. In contrast,
394 structural damage is induced on time scales that are relevant for infection in the range from
395 high pM (>0.4 nM) to nM concentrations.

396
397 **Infection is inhibited at the stage of reverse transcription in the same concentration**
398 **range that is required for efficient capsid rupture in vitro.**
399 Next, we tested whether preincubation of virions with LEN (to allow binding to the capsid to
400 equilibrate prior to cell entry) would result in higher potency of the drug in Jurkat cells
401 infected with VSV-G pseudotyped HIV encoding GFP as a reporter. Similar to the capsid-
402 targeting drug PF74 (Price et al., 2014; Saito et al., 2016), the dose-response curves of LEN
403 showed a biphasic inhibition profile, whereby the first phase (~0.1 nM) reduced infection to
404 about 10% before a second inhibitory mechanism operating in the low nM range reduced
405 infection levels to less than 1% (Figure 5A). Preincubation had little effect on inhibition
406 during the first phase (1.3-fold reduction in IC50, Figure 5–Figure Supplement 1A),
407 consistent with a block at a late stage (e.g. integration) such that the drug had sufficient time
408 to reach the requisite occupancy irrespective of preincubation.
409
410 In contrast to the modest effect at low LEN concentrations, preincubation reduced infection
411 by 2–3-fold at concentrations ≥0.256 nM (i.e., during the second inhibitory phase), whereby
412 the IC95 was 0.5 nM and 1 nM with and without preincubation, respectively (Figure 5A).
413 The increased potency in this range after preincubation is consistent with a mechanism that
414 depends on structural effects on the capsid, that are slow to manifest at sub-nM
415 concentrations as shown above (Figure 4H).
416
417 Next, we determined the dose-dependent effect of LEN on reverse transcription using qPCR
418 with primers amplifying total viral DNA (Figure 5B). The IC50 for reverse transcription in
419 Jurkat cells was 1.08 nM LEN without preincubation, consistent with the dose-response in
420 CEM cells (IC50 = 0.68 nM) (Sowd et al., 2021). This value dropped to 0.59 nM when
421 virions were preincubated for 48 h with LEN prior to infection. Interestingly, the IC50 values
422 for DNA synthesis corresponded to the IC95 values for infection, consistent with a second
423 phase mechanism whereby loss of capsid integrity leads to inhibition of DNA synthesis.
424
425 Finally, the preincubation data allowed us to relate the early- and late-stage inhibition of
426 infection and the inhibition of DNA synthesis to the occupancy of binding sites on the capsid
427 since drug binding equilibrates during the preincubation period before the capsid is exposed
428 to host cofactors. We used the K_D value of the LEN-capsid interaction (0.51 nM, determined
429 above by TIRF imaging) to replot the infection data as a function of occupancy (Figure 5C)
430 and calculate the occupancy at IC50/IC95 for infection and at IC50 for DNA synthesis
431 (Figure 5D). The corresponding plots calculated using the published K_D for the LEN-CA
432 hexamer interaction (0.24 nM) are shown in Figure 5–Figure Supplement 1B and C. From
433 this analysis we conclude that LEN inhibits a late post-entry step when binding to 15% (K_D =
434 0.51 nM) or 30% (K_D = 0.24 nM) of sites, but this block is insufficient to reduce infection
435 below a level of ~10%. At 50% (K_D = 0.51 nM) or 70% (K_D = 0.24 nM) occupancy of sites
436 on the CA lattice, LEN additionally blocks infection by inhibiting reverse transcription,
437 ultimately reducing infection to levels below 1%.
438
439 **LEN and IP6 synergise to promote CA assembly but compete to bias the assembly**
440 **pathway towards tube (LEN) versus cone (IP6) formation.**
441 Since both IP6 (Dick et al., 2018; Renner et al., 2021) and LEN (Bester et al., 2020; Link et
442 al., 2020) promote CA assembly *in vitro*, we tested how the combination of these molecules
443 affects CA assembly in low salt conditions. We monitored the assembly kinetics of
444 recombinant CA by measuring the absorbance at 350 nm and collected samples at the end of
445 each experiment for analysis by negative stain electron microscopy (Figure 6). First, we

446 varied the concentration of IP6 and observed that CA (75 μM) assembled with similar
447 kinetics in the presence of 100 μM or 150 μM IP6 but did not assemble at lower IP6
448 concentrations (Figure 6A, left). As expected, negative stain EM images of assembly
449 products formed with only IP6 showed primarily conical shapes with dimensions similar to
450 those observed for native HIV capsids (Figure 6A, right). When we repeated this titration in
451 the presence of 50 μM LEN (substochiometric relative to CA), we observed CA assembly
452 across the entire concentration range (10–150 μM IP6), with IP6 accelerating assembly
453 kinetics and yields in a concentration-dependent manner (Figure 6B). Strikingly, LEN in the
454 presence of low IP6 promoted formation of CA tubes (often closed at their ends) with lengths
455 of >500 nm, whereby increasing IP6 concentrations biased assembly increasingly towards
456 shorter tubes and conical shapes. Next, we varied the concentration of LEN in the presence of
457 200 μM IP6. Addition of 1–50 μM LEN increased CA assembly efficiency in a
458 concentration-dependent manner above the level observed for IP6 only (Figure 6C, left).
459 Notably, the highest LEN concentration (50 μM) did not promote CA (75 μM) assembly
460 without IP6 in low salt conditions (Figure 6B, left). Negative stain EM images confirmed
461 cone formation in the presence 200 μM IP6 and showed that addition of drug led to the
462 formation of aberrant and broken structures in a concentration-dependent manner (Figure 6C,
463 right). We conclude that LEN is insufficient to promote CA assembly by itself in low salt
464 conditions but synergises with IP6 to increase assembly kinetics and yields. Importantly, IP6
465 promotes cone assembly, whereas LEN biases assembly toward tube formation such that
466 closed tubes form in the presence of high drug and sufficiently low IP6. When both
467 molecules are present at high concentrations, where neither molecule can dominate the
468 assembly pathway, assembly proceeds in an aberrant fashion yielding heterogeneous
469 structures. Taken together these observations show that IP6 and LEN synergise to promote
470 assembly but preferentially stabilise different CA lattice structures.
471
472 **LEN promotes CA overassembly inside mature virions.**
473 As the single-particle TIRF analysis suggested that LEN alters capsid properties inside the
474 intact virion, we used cryo-electron tomography (cryoET) and carried out 3-dimensional
475 reconstructions on untreated and drug-treated (700 nM) virions, which showed the expected
476 distribution of maturation states and capsid shapes (Figure 6–Figure Supplement 1A) as
477 observed before (Fontana et al., 2016; Mallery et al., 2021; Mattei et al., 2014; Renner et al.,
478 2021). The tomograms of LEN-treated virions did not reveal obvious capsid defects (such as
479 large holes), and we were not able to assign small apparent discontinuities as defined holes in
480 the capsid at the resolution of our tomograms. In contrast to untreated virions which
481 contained mostly single capsids comprised of a single CA layer (74%), almost all LEN-
482 treated virions (96%) contained additional CA structures next to the main capsid (61%)
483 and/or appeared with a double layered capsid (45%) (Figure 6–Figure Supplement 1B). These
484 observations suggest that LEN induces assembly of the pool of free CA that is otherwise not
485 incorporated into the capsid. CypA paint analysis of virions pre-treated with 500 nM LEN
486 corroborated this overassembly phenotype, showing an average 1.7–1.8-fold increase of the
487 CypA paint signal (Figure 6–Figure Supplement 1C-E), consistent with the presence of a
488 larger overall CA lattice surface area. Since IP6 is enriched in HIV particles (reaching
489 concentrations of ~500 μM (Mallery et al., 2018)), the drug-cofactor synergy driving aberrant
490 assembly inside virions recapitulates the in vitro assembly data described above. This
491 overassembly defect is likely to play out during capsid assembly in virions produced in the
492 presence of drug, consistent with the observation that virions produced in the presence of
493 LEN (Link et al., 2020) or the closely related compound GS-CA1 (Yant et al., 2019) contain
494 improperly shaped capsids.
495

496
497 **PF74 but not BI-2 slows CA lattice disassembly after capsid rupture.**
498 We have shown before using single-molecule TIRF uncoating assays that PF74, an HIV
499 inhibitor that binds to the same site as LEN, strongly accelerates capsid opening and
500 stabilises the lattice of the capsid thereafter (Márquez et al., 2018). The concentration (10
501 μM) used in those experiments is 40–80-fold above the K_D determined for the interaction
502 with CA hexamers (between 0.12 μM (Price et al., 2014) to 0.26 μM (Bhattacharya et al.,
503 2014)), such that 97–99% of binding sites of the capsid are predicted to be occupied with a
504 drug molecule. PF74 is an important tool to study HIV capsid-associated processes but has
505 been described to either promote capsid uncoating (Santos et al., 2016; Selyutina et al., 2022;
506 Shi et al., 2011) or to stabilise capsids (Rankovic et al., 2018) or to have no effect on capsid
507 integrity (Hulme et al., 2015). To resolve this ambiguity and further characterise the ability of
508 PF74 to stabilise (broken) CA lattices, we carried out CypA paint experiments in the presence
509 of 0.1–10 μM PF74 (Figure 7A). In this concentration range, binding quickly reaches
510 equilibrium and occurs before membrane permeabilization in our assay. PF74 slowed the loss
511 of CA from leaky and opening capsids in a concentration-dependent manner. Maximum
512 stabilisation required essentially all sites to be drug-bound (97–99% at 10 μM), but even at
513 this occupancy we observed ~70% signal loss after 80 min (Figure 7B). Thus, PF74 was
514 unable to prevent CA lattice disassembly to the same extent as LEN (Figure 3E). PF74 also
515 required near saturating occupancy to accelerate capsid opening, and at a concentration of 1
516 μM (79–89% occupancy), the drug showed only partial capsid-breaking activity (Figure 7–
517 Figure Supplement 1).
518
519 The FG pocket-binding drug BI-2 also has potent capsid-breaking activity (Márquez et al.,
520 2018) when used at a concentration (50 μM) that is ~40-fold above the K_D (1.2 μM) of the
521 interaction with CA hexamers (Price et al., 2014). We predicted that BI-2 would be unable to
522 stabilise CA lattices after capsid opening since the compound contacts only one of the two
523 CA subunits forming the FG binding pocket (Figure 1A). As expected, CypA paint analysis
524 showed that 50 μM BI-2 did not slow the release of CA subunits from the lattice (Figure 7E).
525 These observations together with those described above suggest that PF74 exerts the same
526 structural effects on the capsid as LEN but less potently, while BI-2 breaks the capsid but is
527 unable to slow subsequent disassembly.
528
529 To relate the degree of the capsid-altering effects of PF74 to its effects on HIV infection, we
530 measured the dose-response curve for inhibiting infection of Jurkat cells with VSV-G
531 pseudotyped HIV encoding GFP as a reporter (Figure 7C). The curve showed the
532 characteristic biphasic profile with the first phase levelling off at ~10% infection at ~1 μM
533 followed by a second drop in infection above 4 μM. To facilitate comparison to the
534 corresponding biphasic LEN data, we replotted the infection data as a function of occupancy
535 (Figure 7D). Compared to LEN, the PF74 curve was shifted to higher occupancies, whereby
536 late phase inhibition with PF74 required >95% occupancy, i.e. the same as required for
537 stabilisation of open CA lattices (Figure 7A). In comparison, LEN required between 35–70%
538 occupancy for late phase inhibition (Figure 5C and Figure 5–Figure Supplement 1B), again
539 corresponding to the level required for CA lattice stabilisation (Figure 3E). Taken together,
540 our CypA paint and infection data show that LEN can elicit the detrimental capsid structural
541 changes characteristic of the second phase at lower occupancy than PF74.
542
543 **CPSF6 peptide stabilises the CA lattice at low occupancy.**
544 Given that different compounds can influence uncoating mechanisms in different ways, it is
545 conceivable that the virus uses endogenous ligands to tune capsid stability. We therefore

546 sought to compare the effect of the above drugs with CPSF6, a host cell protein which also
547 binds the FG-pocket, and bridges the gap between monomers (Price et al., 2012). CPSF6
548 colocalises with the capsids at the nuclear pore complex and inside the nucleus where it plays
549 a role in facilitating nuclear entry and dictating integration site position (Bejarano et al.,
550 2019; Schaller et al., 2011; Sowd et al., 2016; Zila et al., 2021). To investigate the effect of
551 CPSF6 on capsid stability, we performed single-molecule TIRF uncoating experiments in the
552 presence of the minimal CPSF6 peptide that binds to the FG pocket (Figure 1D). At 100 μM
553 (2–fold above the KD of 50 μM for binding to CA hexamers), CPSF6 peptide promoted
554 capsid opening, but with slower kinetics than the FG pocket-binding drugs (Figure 8–Figure
555 Supplement 1). CypA paint analysis showed that 100 μM CPSF6 peptide strongly inhibited
556 CA release (Figure 8A) as evident from slow decay in the CypA paint signal over 80 min
557 (Figure 8C). Further, 1 μM CPSF6 peptide (6% occupancy, Figure 8B) was insufficient to
558 stabilise the lattice but 5 μM (18.5% occupancy, Figure 8B) partially and 10 μM (<50%
559 occupancy) strongly inhibited CA lattice dissociation. Thus, CPSF6 peptide was similarly
560 stabilising relative to occupancy to LEN and more potent than PF74 and BI-2, providing
561 partial stabilisation when fewer than 20% of binding sites are occupied.
562

563 **Discussion**

564 Here we show that the antiretroviral LEN has two opposing effects on the HIV-1 capsid at
565 high occupancy: it prevents dissociation of CA from the lattice but induces capsid rupture.
566 This apparently counterintuitive phenomenon is consistent with a model in which the lattice
567 must be simultaneously stable but flexible. The antiviral mechanism of LEN can therefore be
568 considered a form of 'lethal hyperstability' in which lattice stability is increased at the cost of
569 its flexibility and ultimately capsid integrity. This is reminiscent of the 'lethal mutagenesis'
570 mechanism of antiviral polymerase drugs such as favipiravir (Perales et al., 2011). Just as
571 with capsid stability, viral replication has conflicting requirements – errors are necessary to
572 promote mutagenesis and evolvability (Tokuriki and Tawfik, 2009) but too many errors and
573 fidelity is compromised. Lethal mutagenesis drugs exert their antiviral affects by pushing
574 viral polymerases to these unsustainable error rates. Similarly, lethal hyperstability capsid
575 drugs like LEN push the capsid lattice to extremely stabilised structures that are incompatible
576 with capsid integrity. Importantly, this mechanism dominates at drug doses required to
577 suppress replication to clinically relevant levels (Dvory-Sobol et al., 2022).
578

579 The effects of lethal hyperstability are observable prior to reaching binding equilibrium or
580 full occupancy and we estimate that efficient and rapid drug-induced capsid rupture and
581 lattice stabilisation occurs when half of the binding sites are occupied. The overall kinetics of
582 inducing structural effects depend on LEN binding kinetics and occupancy-dependent
583 structural changes. As occupancy increases over time, breakage becomes increasingly likely
584 and rapid. Due to the high affinity of the drug, sub-nM concentrations are sufficient to induce
585 structural effects, but it takes hours to reach the requisite binding level. The cofactor IP6,
586 which, in the absence of drug, would normally delay spontaneous capsid opening by many
587 hours, counteracts but is ultimately unable to prevent LEN-induced capsid rupture. It is also
588 worth noting that HIV capsids are pleiomorphic and exhibit different levels of intrinsic
589 stability as evident from our single-particle analysis, such that the occupancy required for
590 LEN-induced structural changes is likely to vary between different capsid architectures.
591

592 The comparison of the single-particle analysis of the three major drugs (BI-2, PF74, and
593 LEN) offers insight into how binding stabilises the CA lattice, even when it is no longer a
594 closed shell. BI-2 is the simplest compound, and only makes contacts within a single
595 monomer and has the lowest affinity. As such it offers no potential for enhancing contacts

596 between individual proteins within the lattice. It is therefore unsurprising that, even at 50 μM
597 (approaching the solubility limit of the drug), BI-2 provides no significant lattice stabilisation
598 once the capsid has ruptured. PF74 and LEN, on the other hand, both make contacts across
599 the junction between monomers within the context of the hexamer, and both have been
600 shown to have higher affinity for hexamers than monomers. This suggests that the two drugs
601 lock monomers together within the hexamer, potentially limiting their ability to move with
602 respect to each other - reducing degrees of freedom and hence flexibility within the lattice
603 that is required to maintain a closed capsid. Evidence that the hexamers are stabilised comes
604 from lattice assembly experiments in which LEN promotes CA assembly in the presence of
605 IP6 (Figure 6) or high salt (Bester et al., 2020; Link et al., 2020). While PF74 does stabilise
606 the CA lattice post-rupture, the lattice will deteriorate on a time scale of an hour. LEN-treated
607 cores, on the other hand, show no lattice loss even after 5 hours post-rupture. The degree of
608 lattice stabilisation, therefore, correlates with the degree to which the drugs bridge the
609 junction between monomers.
610
611 How exactly stabilising the lattice triggers capsid rupture is less clear. It has previously been
612 suggested that the binding of the drug reduces the flexibility of the CA molecule and
613 therefore the lattice plasticity required to maintain capsid integrity (Bhattacharya et al.,
614 2014). These authors also suggest that, due to its hexamer preference, PF74 stabilises
615 hexamers at the cost of pentamers. As precisely 12 pentamers are required, any process that
616 disfavour pentamers, would necessarily lead to capsid rupture. A recent cryoEM study
617 comparing the structures of hexamers and pentamers identified residues 58-61 as being a
618 potential 'switch' between the two states (Schirra et al., 2023); this switch was also
619 confirmed in a second cryoEM study (Stacey et al., 2023). Importantly, the pentamer
620 configuration of these residues results in a remodelling of the FG-binding site. The authors
621 speculate that LEN may result in an induced fit switch to the hexameric configuration
622 (Schirra et al., 2023), and our data would be consistent with such a model. Another cryoET
623 study of HIV cores incubated under conditions that facilitate reverse transcription inside the
624 capsid showed that treatment with GS-CA1 (an analogue of LEN) for 4 hours led to loss of
625 CA lattice pieces and a flattening of the remaining lattice (Christensen et al., 2020). The
626 authors proposed that the compound restricts CA flexibility, causing a build-up of lattice
627 strain, and consequently lattice fracture. We previously proposed a similar mode of action for
628 the capsid-breaking activity of PF74 (Márquez et al., 2018). Finally, cryoEM of templated
629 CA lattices confirmed that LEN binds exclusively to hexamers and suggested a critical role of
630 IP6 for the formation of pentamers and high curvature (Highland et al., 2023), consistent with
631 our observation that IP6 can partially antagonise LEN-induced rupture of the closed cone.
632
633 LEN also possesses antiviral activity during viral production. Not only does LEN
634 compromise the integrity of existing capsid cores but it interferes with assembly/maturation
635 as well. Our *in vitro* assembly experiments suggest that, while LEN promotes IP6-driven
636 assembly it leads to improperly assembled cones that cannot be closed. This is consistent
637 with the observation that LEN (Bester et al., 2020) and the closely related analogue GS-CA1
638 (Yant et al., 2019) lead to the formation of aberrant capsids in virions. IP6 binds to the
639 electropositive 'pore' created by 6 (or 5) copies of Arg18 at the centre of each CA hexamer
640 (or pentamer). By neutralising the charge repulsion, IP6 stabilises these structures and is
641 thought to be particularly important for incorporation of pentamers (Gupta et al., 2022;
642 Renner et al., 2021) required for forming the high curvature lattice at the ends of the cone. On
643 the other hand, LEN drives assembly of low curvature hexameric lattices (Figure 6B). Both
644 compounds together might lead to uncontrolled lattice growth without the ability to reverse
645 defects and/or LEN might drive remodelling of pentamers at the growing lattice edge into

646 hexamers (Grime et al., 2016). Furthermore, the over-assembly phenotype that we observe
647 upon drug treatment of mature virions supports the notion that LEN causes aberrant CA
648 assembly in addition to distorting existing structures. While our data do not resolve how the
649 LEN-induced capsid defects manifest structurally in isolated capsids, within mature virions
650 this could be due to a build-up of strain within the primary capsid. In addition, 'secondary CA
651 lattices' would likely compete for the limited IP6 present within the virion, effectively
652 reducing the amount available to the primary capsid, thereby reducing its resistance to rupture
653 and possibly also adjusting the hexamer/pentamer balance.
654
655 The antiviral multimodality of LEN is also seen in the biphasic response curve in the
656 infection assay. The high-dose phase occurs above 0.5 nM LEN, above which the
657 considerations of capsid rupture are relevant. The high-dose phase also corresponds to the
658 concentrations at which reverse transcription is also inhibited. A biphasic inhibition curve has
659 previously been seen for PF74 (and is repeated here) where, similarly, loss of reverse
660 transcription accompanies this high-dose phase. We and others had previously attributed the
661 loss of reverse transcriptase activity to the opening of the capsid lattice and release of the RT
662 enzyme (Christensen et al., 2020; Jennings et al., 2020; Sowd et al., 2021). Our data support
663 this same explanation for LEN-induced loss of RT. However, LEN is not simply a tighter-
664 binding version of PF74. Figure 5C (LEN) and Figure 7D (PF74) show that when the drug
665 response curves are plotted as a function of occupancy, LEN exerts its effects at much lower
666 capsid occupancy than PF74. In a previous study, when BI-2 and PF74 were similarly
667 compared, they were found be identical (Price et al., 2014). This suggests that increased CA
668 affinity only partially explains LEN's superior potency and may speak to a greater
669 'rigidification potential' or ultrastructure-altering capability relative to prior compounds that
670 target this same site.
671
672 While the second phase of the dose response curve has a clear explanation, the activity of the
673 drugs at the first phase remains controversial. At these concentrations (<0.5 nM for LEN; <4
674 nM PF74, <50 nM for BI-2) neither capsid rupture nor loss of viral DNA synthesis are
675 observed. One possible explanation could be that at low drug concentration the low
676 occupancy contributes to CA lattice stability, without the concomitant rupture observed at
677 higher doses. In combination with the cone-stabilising activity of IP6, low dose LEN could
678 render the capsid core too stable thereby leading to altered genome release kinetics during
679 infection. However, the observation that 2-LTR circle formation is not reduced at the EC50
680 for infection (Bester et al., 2020) is inconsistent with this model as failure to release the viral
681 cDNA from the capsid would be expected as a result of capsid stabilisation. Alternatively,
682 disrupting the ability of the capsid to interact with FG-containing cofactors (Sec24C,
683 Nup153, and CPSF6) has also been proposed to inhibit infection. Our data predict that, at its
684 EC50, LEN occupies approximately one third of the FG-binding sites, while PF74 occupies
685 >80% of sites (Figure 7D). However, the true degree to which these drugs are able to
686 compete with cofactor binding during infection is complicated by the spatial organisation of
687 the cofactors in the cell, the unknown degree to which they compete with each other, the
688 possibility that they exist as high-avidity multimers , and fluctuations in their abundances
689 throughout the cell cycle and between cell types (Wei et al., 2022).
690
691 The fact that these drugs target a cofactor binding site (the FG pocket) and are capable of
692 modulating capsid rupture and stability raises the question as to whether the virus is
693 employing these cofactors to regulate uncoating. This has previously been suggested for
694 cofactors binding at other CA lattice sites, such as the interactions between CypA and the
695 cyclophilin loop (Rasaiyaah et al., 2013) or between IP6 and the R18 ring (Mallery et al.,

2018). The best characterised of the cofactors interacting with the FG pocket is CPSF6, which binds via a linear peptide motif and, like PF74 and LEN makes contacts across the junction between monomers. Our observation that CPSF6 stabilises the CA lattice is consistent with the notion that this bridging interaction promotes stability. A surprising result was the degree to which CPSF6 provided stabilisation, achieving this effect as low as 20% binding sites are occupied. This could indicate that the nature of the bridging interaction is somehow more flexible than those observed for the drugs, leading to differences in the dependence of binding on the curvature of the CA lattice. Indeed, cryoET imaging of CA cones have shown that CPSF6 binding is independent of lattice curvature (Stacey et al., 2023) while PF74 prefer low curvature regions (Lu, 2020). We acknowledge that we are studying an isolated monomeric peptide motif, while endogenous CPSF6 will likely have a higher binding constant due to avidity, as it is expected to be at least a dimer (Ning et al., 2018), but possibly higher, as CPSF6 has been associated with phase separated condensates within the nucleus (Greig et al., 2020). The nuclear localisation of CPSF6 and the above stabilisation activity, may account for the observation of capsid remnants in the nucleus discrete from integrated proviral DNA (Müller et al., 2021; Zila et al., 2021).

For decades, the concept that the HIV capsid must release its contents to complete infection has been accepted, and the metastability of the capsid has been recognised as critical for the viral life cycle. LEN is the first capsid-targeting drug for treatment of HIV infection. Our work here shows that LEN functions by lethal hyperstabilisation, and that this is a powerful mechanism for achieving multi-log impacts on viral infectivity. As such, this mechanism and the tools that we and others have developed for studying it will likely be relevant to the development of new therapeutics targeting a range of viral infections. Furthermore, LEN reveals that FG-pocket binding can drastically alter the capsid integrity. The exact nature of the induced ultrastructural defect warrants further study, as does the role of single and multiple endogenous cofactors on the uncoating process.

724 # Materials and Methods
725 **Cell lines**
726 HEK-293T cells and Jurkat cells were obtained from ATCC. Identity testing was carried out
727 by PCR. Cell lines tested negative for mycoplasma.
728
729 **Production of GFP-loaded HIV particles for TIRF uncoating experiments**
730 HIV particles lacking envelope protein were produced, biotinylated and purified as described
731 (Márquez et al., 2019). Briefly, HEK-293T cells were transfected using PEI with a mixture of
732 the plasmids pNL4.3-iGFP-ΔEnv and psPAX2 (1.4:1, mol/mol) to produce GFP-loaded HIV
733 particles or with a mixture of pCRV1-GagPol and pCSGW (1:1.7, mol/mol) to produce dark
734 HIV particles. The medium was exchanged 18 h post transfection and the virus-containing
735 medium was collected 72 hours post transfection and centrifuged (2100 x g, 20 min, 4 °C) to
736 remove cells. The viral particles were then biotinylated using EZ-Link Sulfo-NHS-LC-LC-
737 Biotin and purified by size exclusion chromatography.
738
739 **Expression and purification of DLY**
740 The gene encoding the pore-forming protein desulfolysin (DLY) was subcloned by ligation
741 independent cloning into the pMCSG7 vector from the pET22b construct described in (Hotze
742 et al., 2013) to introduce an N-terminal His-tag. DLY was expressed in *E. coli* BL21(DE3)
743 pREP4 cells in TB media with Ampicillin (100 mg/mL) by induction with 0.2 mM IPTG at
744 37 °C with shaking for 4 hours. Cells were harvested by centrifugation and lysed in 20 mM
745 Tris pH 7.2 300 mM NaCl buffer with 10% glycerol, protease inhibitor, 0.1% Triton-X100,
746 DNAse and lysozyme for 1 hour at room temperature. The lysate was clarified by
747 centrifugation and passed over a HisTrap™ HP column (Cytiva Life Sciences) equilibrated in
748 20 mM Tris pH 7.2, 300 mM NaCl and 5% glycerol. DLY was elutded over a linear gradient
749 of 0–500 mM imidazole. The eluted protein was further purified by size exclusion
750 chromatography on a HiLoad 16/60 Superdex 200 pg column (Cytiva Life Sciences)
751 preequilibrated with 20 mM Tris pH 7.2, 300 mM NaCl, 5% glycerol, 0.5 mM DTT.
752
753 **Expression and purification of CypA**
754 Human CypA was expressed in BL21(DE3) *E. coli* for 3 h after IPTG induction in LB
755 medium at 37 °C with shaking. Cells were harvested by centrifugation and lysed by
756 sonication on ice in a buffer containing 25 mM HEPES, pH 7.6, 1 mM DTT, 0.02% NaN_3,
757 'Complete' protease inhibitor and 1 mg mL^{-1} lysozyme. The lysate was clarified by
758 centrifugation. CypA was purified by subtractive anion exchange chromatography using a 10
759 mL HiTrap Q HP column (GE Healthcare Life Science) equilibrated with 25 mM HEPES,
760 pH 7.6, 1 mM DTT, 0.02% NaN_3. CypA fractions eluting in the flow-through were adjusted
761 to pH of with 1% v/v acetic acid, centrifuged and applied to a cation exchange
762 chromatography column (5 mL HiTrap SP HP, GE Healthcare Life Science) equilibrated
763 with 25 mM sodium phosphate, pH 5.8, 1 mM DTT, 0.02% NaN_3. CypA was eluted with a
764 linear gradient from 0 to 1 M NaCl over 20 column volumes. CypA was dialyzed against
765 storage buffer (25 mM MOPS, pH 6.6, 1 mM DTT, 0.02% NaN_3), concentrated using an
766 Amicon-15 Ultra centrifugal filtration device (10 k MWCO, Merck) and frozen in liquid
767 nitrogen for storage at -80 °C.
768
769 **Labelling of CypA**
770 CypA was dialysed against PBS (pH 7.4, 0.1 mM TCEP) and labeled by reaction with a 4-
771 fold molar excess of Alexa-Fluor 568-C5-maleimide (Thermo Fisher Scientific, A10254) for
772 10 minutes at room temperature. The reaction was quenched by addition of DTT. Labeled
773 CypA was separated from unconjugated dye using Zeba desalting spin columns (Thermo

774 Fisher Scientific) equilibrated with 50 mM Tris, pH 7.9, 20% v/v glycerol, 1 mM DTT.
775 Under these conditions, CypA is quantitatively labeled at residue C51. Labeled CypA was
776 frozen in liquid nitrogen and stored at -40 °C.
777
778 **CPSF6 peptides**
779 The peptides $CPSF6_{313–327}$ (CPSF6p) and $CPSF6_{313–327}$ with an extra cysteine at the C-
780 terminus (CPSF6p-Cys) were synthetized by GenScript. Peptides were dissolved in water at a
781 concentration of 2.5 mM and stored in aliquots at -40°C.
782
783 **Labelling of CPSF6 peptide**
784 CPSF6p-Cys was labelled with Alexa-Fluor 568-C5-maleimide (Thermo Fisher Scientific)
785 added at an equimolar ratio in HEPES buffer pH 8. Labelling was verified by thin layer
786 chromatography (TLC). No unconjugated dye was observed on TLC. CPSF6p-Cys- AF568
787 solution stored in aliquots at -40°C.
788
789 **Single-molecule TIRF uncoating assay**
790 Single-molecule imaging of viral particles was carried out using TIRF microscopy with
791 microfluidic sample delivery according to our previously published methods (Márquez et al.,
792 2019). Briefly, biotinylated viral particles were captured onto coverslips attached to PDMS
793 microfluidic flow cells and imaged using a custom-built TIRF microscope with an ASI-
794 RAMM frame (Applied Scientific Instrumentation), a Nikon 100× CFI Apochromat TIRF
795 (1.49 NA) oil immersion objective and NicoLase laser system (Nicovich et al., 2017).
796 Immobilized virions were treated with imaging buffer containing 200 nM pore forming
797 protein (DLY or SLO) to permeabilize viral membrane and AF568-labeled CypA (0.8 μM) to
798 paint the capsid. Drugs (LEN, PF74, BI-2) were added to the imaging buffer as stock
799 solutions in DMSO (final concentration not exceeding 0.5%). Images were acquired at a rate
800 of 1 frame per 6 s for 30 minutes unless specified otherwise.
801
802 **TIRF image analysis**
803 Single-virion fluorescence traces were extracted from the TIRF image stacks using the JIM
804 Immobilized Microscopy analysis package (JIM v7, freely available at
805 https://github.com/lilbutsa/JIM-Immobilized-Microscopy-Suite) and further analyzed in
806 MATLAB (The MathWorks Inc.). *Capsid opening via GFP release:* Change-point analysis
807 of GFP intensity traces using an algorithm (Taylor, 2000) implemented in C++ was used to
808 identify the presence and time of steps corresponding to membrane permeabilization and
809 capsid opening. Step probabilities were calculated non-parametrically using 10,000 bootstrap
810 iterations. Step times were calculated using least squares fitting. Traces were automatically
811 sorted into four classes based on the following criteria: (1) loss of entire GFP signal in one
812 step; (2) loss of GFP intensity in one large step (permeabilization) and one small step (capsid
813 opening, identified with ≥75% step probability and ≥75% signal loss); (3) loss of the majority
814 of the GFP signal in one step with residual GFP signal persisting for the rest of the
815 experiment; (4) no or insufficient GFP signal drop or traces with more than two steps
816 (excluded from analysis). Capsid opening times were calculated for traces in class two as the
817 time difference between permeabilization and capsid opening. Survival curves were
818 constructed from the pooled opening times acquired in independent uncoating experiments.
819 *Analysis of CA lattice stability via CypA paint:* Heatmaps and median traces of leaky or
820 closed particles were generated after aligning at traces in the corresponding category at the
821 time of membrane permeabilization. Traces of opening particles were aligned at the time of
822 membrane permeabilization (shown in the first panel) and aligned at the time of capsid
823 opening (shown in the second panel). *Quantification of bound molecules:* The number of

824 bound AF568-labelled CPSF6p molecules was determined by dividing the CPSF6p-AF568
825 fluorescence intensity associated with each capsid by the fluorescence intensity of a single
826 CPSF6p-AF568 molecule. The fluorescence intensity of the single fluorophore was
827 determined from the quantal photobleaching step in photobleaching traces of CPSF6p-AF568
828 molecules adsorbed sparsely to the coverslip surface and imaged continuously.
829
830 **Calculation of occupancy**
831 The occupancy at equilibrium (θ_{eq}) of FG binding pockets on the capsid with LEN was
832 calculated using the equation $\theta_{eq} = c_{LEN} / (c_{LEN} + K_D)$, where c_{LEN} is the LEN concentration
833 and K_D is the dissociation constant of the LEN-capsid interaction. The occupancy as a
834 function of time ($\theta(t)$) was calculated using the following equation: $\theta(t) = \theta_{eq}(1\text{-exp}(-$
835 $(k_{on} \times c_{LEN} + k_{off}) \times t)$, where θ_{eq} is the occupancy at equilibrium, c_{LEN} is the LEN
836 concentration, k_{on} is the association rate constant and k_{off} is the dissociation rate constant.
837 Estimates for K_D, k_{on} and k_{off} were obtained from TIRF imaging in this work (K_D = 1 nM, k_{on}
838 = 1.84E5 $M^{-1}s^{-1}$ and k_{off} = 1.84E-4 s^{-1}) or from published values obtained by surface plasmon
839 resonance spectroscopy (K_D = 0.24 nM, k_{on} = = 6.5E4 $M^{-1}s^{-1}$ and k_{off} = 1.4E-5 s^{-1}) (Link et al.,
840 2020).
841
842 **Production of pseudotyped-virus particles for cell-based assays**
843 VSV-G pseudotyped GFP-encoding virus particles were generated by co-transfecting
844 HEK293T cells with pCRV1-GagPol, pCSGW and pMD2.G (1:1.1:1.3 mol/mol) using PEI
845 25K. The culture medium was removed 16 hours post-transfection and replenished with a
846 fresh medium containing 10 mM $MgCl_2$, 0.5 mM $CaCl_2$ and 100 U of DNase. Virus-
847 containing medium was harvested 72 hours post-transfection, centrifuged (2100 x g, 20 min,
848 4°C) to remove cell debris, divided into aliquots and stored at -80°C.
849
850 **Infection assays**
851 Infection assays were performed in 96 well plates using 0.75 x 10^5 Jurkat cells per well pre-
852 treated with the indicated drug (LEN, PF74) concentrations for 30 minutes at 37°C. The cells
853 were then infected in triplicate with VSV-G-pseudotyped GFP-encoding virus in the presence
854 of polybrene (10 µg/ml; Sigma) at room temperature for 20 minutes, followed by
855 spinoculation at 800 x g for 1 hour at room temperature. The culture media were removed
856 and replenished with fresh media containing drugs at the indicated concentrations. At 48
857 hours post infection, the cells were fixed in 2% paraformaldehyde (Electron Microscopy
858 Sciences) for 1 hour at room temperature and analyzed by flow cytometry using a
859 LSRFortessa cell analyzer (BD Biosciences) and FlowJo software. For experiments involving
860 preincubation with drugs, the virus was incubated with LEN at the indicated concentrations
861 for 48 hours at room temperature and then used to infect cells as above. We chose 48 h
862 because this time is sufficient for binding at concentrations ≥50 pM to reach ≥95% of the
863 respective equilibrium level (Figure 4–Figure Supplement 1A). For quantitative PCR (qPCR)
864 analysis, virus was treated with DNase for 30 minutes at 37°C and then used to infect 1 x 10^5
865 Jurkat cells in duplicate as described above. Cells were harvested 24 hours post infection and
866 processed for qPCR.
867
868 **Quantitative PCR analysis**
869 Genomic DNA was isolated from pelleted cells using a DNeasy blood and tissue kit
870 (Qiagen). The concentration of purified DNA was determined using a Nanodrop
871 spectrophotometer. To quantify total viral DNA, quantitative PCR was performed using
872 sequence-specific primers and SsoAdvanced Universal SYBR Green Supermix (Bio-Rad).
873 For 2-LTR circles, quantitative PCR was performed using sequence-specific primers,

874 TaqMan probes (Thermo Fisher Scientific) and iQ Supermix (Bio-Rad). PCR conditions for
875 vDNA amplification: Initial denaturation, 95ºC, 3 min; Denaturation, 95ºC, 10 s;
876 Annealing/Extension, 60ºC, 30 s; 45 cycles. PCR conditions for 2-LTR amplification: Initial
877 denaturation, 95ºC, 3 min; Denaturation, 95ºC, 15 s; Annealing/Extension, 60ºC, 60 s; 50
878 cycles.
879
880 **Expression and purification of CA for in vitro assembly experiments**
881 *E. coli* C41 cells expressing CA were lysed and cell debris was removed by centrifugation.
882 CA was precipitated by addition of 25% ammonium sulphate to the supernatant, collected by
883 centrifugation, resuspended, and dialysed against 50 mM MES (pH 6.0), 20 mM NaCl, 1 mM
884 DTT. The CA protein was further purified on a cation exchange column with a gradient from
885 20 mM to 1 M NaCl followed by size exclusion chromatography with Tris pH 8.0, 20 mM
886 NaCl, 1 mM DTT and finally snap frozen.
887
888 **Turbidity assay to measure CA assembly kinetics**
889 CA proteins were dialysed against 50 mM MES (pH 6.0), 1 mM DTT. CA proteins were
890 assembled at a final concentration of 75 µM in the presence of 2% DMSO. LEN titration:
891 LEN (final concentration between 0.5–50 µM) was added to the CA solution and assembly
892 was initiated by adding IP6 (final concentration of 200 µM). IP6 titration: IP6 (final
893 concentration between 50–150 µM) ±LEN (final concentration 50 µM) was added to the CA
894 solution to induce assembly. The increase in Abs_{350} was measured with a PHERAstar FSX
895 Plate reader (BMG Labtech) in 384-well plate every 22 s with shaking after each
896 measurement.
897
898 **Treatment of self-assembled CA cones with LEN**
899 CA cones were assembled by adding IP6 (final concentration of 1 mM) to a solution of CA
900 (final concentration of 75 µM) in 50 mM MES (pH 6.0) and incubating the reaction mixture
901 for 2 h. LEN (final concentration of 50 µM) was added and the CA cones and the mixture
902 was applied to an EM grid for negative staining with uranyl acetate at the indicated time
903 points.
904
905 **Negative staining EM of self-assembled CA structures**
906 The samples from the turbidity assay were allowed to sediment overnight. Then 5 µL of each
907 sample was applied to a carbon coated grid (Cu, 400 mesh, Electron Microscopy Services)
908 previously cleaned by glow discharge. The grids were then washed, and samples stained with
909 2% uranyl-acetate. Micrographs were taken at room temperature on a Tecnai Spirit (FEI)
910 operated at an accelerated voltage of 120 keV and recorded with a Gatan 2k × 2k CCD
911 camera. Images were collected with a total dose of ~30 $e^-/Å^2$ and a defocus of 1–3 µm.
912
913 **HIV particle production for cryo-electron tomography**
914 Replication deficient VSV-G pseudotyped HIV-1 virions were produced in HEK293T cells
915 using pCRV1-GagPol, pCSGW and pMD2.G as described previously (Price et al., 2014). At
916 24–48 h post transfection, the supernatants were harvested and passed through 0.22 µm
917 nitrocellulose filter. The virions were concentrated by ultracentrifugation through a 20%
918 (w/v) sucrose cushion (2 h at 28,000 rpm in a SW32 rotor [Beckman Coulter Life Sciences]).
919 The pellet was resuspended in PBS, snap-frozen and stored at -80 °C. LEN-treated virions
920 were incubated in presence of 700 nM LEN for 1.5 h at room temperature prior to plunge-
921 freezing for cryo-ET.
922
923 **Cryo-electron tomography of LEN-treated HIV particles**

Colloidal gold beads (10 nm diameter) were added to the purified HIV particles and 6 µl of this suspension was applied to a C-Flat 2/2 3C grid cleaned by glow discharge (20 mA, 40 s). The grids were blotted and plunge-frozen in liquid ethane using an FEI Vitrobot Mark II at 16 °C and 100% humidity. Tomographic tilt series between −40° and +40° with increments of 3°, defoci between -3 µm and -6 µm at a magnification of 50,000x were acquired using Serial-EM (Mastronarde, 2005) on a TF2 Tecnai F20 transmission electron microscope under low-dose conditions at 200 kV and images recorded with a Falcon III direct electron detector. The Imod package (IMOD Version 4.9.0) was used to generate tomograms (Kremer et al., 1996). The alignment of 2D projection images of the tilt series was done using gold particles as fiducial markers. A 3D reconstruction was generated using back projection of the tilt-series. All the morphological classes, including the double-layered capsids, were classified by visual inspection.

Acknowledgements

This work was supported by NHMRC Ideas Grant APP1182212 (DAJ, TB), Wellcome Trust Collaborator Award 214344/Z/18/Z (GJT, LJ, DAJ, TB), NHMRC Investigator Grant APP1194263 (MWP), Australian Research Council Grants DP160101874 and DP200102871 (MWP) and a UNSW Scientia Award (KMRF). CM received an Australian Government Research Training Program Scholarship. Infrastructure support from the NHMRC Independent Research Institutes Infrastructure Support Scheme and the Victorian State Government Operational Infrastructure Support Program to St. Vincent's Institute are gratefully acknowledged. MWP is an NHMRC Leadership Fellow. We thank Sara Lawrence (St. Vincent's Institute) for expression and purification of recombinant DLY, Claire Dickson and Prabhjeet Phalora for critical feedback on the manuscript.

Author contributions

K.M. Rifat Faysal: Methodology; Investigation; Formal analysis; Writing-Original draft.
James Walsh: Methodology; Investigation; Formal analysis; Writing–review and editing
Nadine Renner: Investigation; Formal analysis; Writing–review and editing
Chantal Márquez: Investigation; Formal analysis; Writing–review and editing
Vaibhav Shah: Investigation; Formal analysis; Writing–review and editing
Andrew Tuckwell: Formal analysis; Writing–review and editing
Michelle Christie: Resources; Writing–review and editing
Michael Parker: Resources; Writing–review and editing; Supervision; Funding acquisition
Stuart Turville: Resources; Writing–review and editing; Supervision; Funding acquisition
Greg Towers: Writing–review and editing; Funding acquisition
Leo James: Writing–review and editing; Supervision; Funding acquisition
David Jacques: Conceptualisation; Writing–original draft; Supervision; Funding acquisition
Till Böcking: Conceptualisation; Methodology; Writing–original draft; Supervision; Funding acquisition

ORCID IDs

James Walsh: 0000-0003-0447-2323
Chantal Márquez: 000-0002-3935-4554
Vaibhav Shah: 0000-0002-9123-0180
Andrew Tuckwell: 0000-0002-8940-7768
Michelle Christie: 0000-0002-7001-3400
Michael Parker: 0000-0002-3101-1138
Stuart Turville: 0000-0003-1918-5343
Greg Towers: 0000-0002-7707-0264
Leo James: 0000-0003-2131-0334
David Jacques: 000-0002-6426-4510
Till Böcking: 0000-0003-1165-3122

981 # References
982
983

984 Alvarez LZ, Govasli ML, Rasaiyaah J, Monit C, Perry SO, Sumner RP, McAlpine-Scott S, Dickson C,
985 Faysal KMR, Hilditch L, Miles RJ, Bibollet-Ruche F, Hahn BH, Boecking T, Pinotsis N, James LC,
986 Jacques DA, Towers GJ. 2022. Macrophage activation of cGAS and TRIM5 distinguish pandemic
987 and non-pandemic HIV. *Biorxiv* 2022.01.21.477263. doi:10.1101/2022.01.21.477263

988 Bejarano DA, Peng K, Laketa V, Börner K, Jost KL, Lucic B, Glass B, Lusic M, Müller B, Kräusslich H-
989 G. 2019. HIV-1 nuclear import in macrophages is regulated by CPSF6-capsid interactions at the
990 nuclear pore complex. *Elife* **8**:e41800. doi:10.7554/elife.41800

991 Bester SM, Wei G, Zhao H, Adu-Ampratwum D, Iqbal N, Courouble VV, Francis AC, Annamalai AS,
992 Singh PK, Shkriabai N, Blerkom PV, Morrison J, Poeschla EM, Engelman AN, Melikyan GB, Griffin
993 PR, Fuchs JR, Asturias FJ, Kvaratskhelia M. 2020. Structural and mechanistic bases for a potent
994 HIV-1 capsid inhibitor. *Sci New York N Y* **370**:360–364. doi:10.1126/science.abb4808

995 Bhattacharya A, Alam SL, Fricke T, Zadrozny K, Sedzicki J, Taylor AB, Demeler B, Pornillos O,
996 Ganser-Pornillos BK, Diaz-Griffero F, Ivanov DN, Yeager M. 2014. Structural basis of HIV-1 capsid
997 recognition by PF74 and CPSF6. *Proceedings of the National Academy of Sciences* **111**:18625–
998 18630. doi:10.1073/pnas.1419945112

999 Blair WS, Pickford C, Irving SL, Brown DG, Anderson M, Bazin R, Cao J, Ciaramella G, Isaacson J,
1000 Jackson L, Hunt R, Kjerrstrom A, Nieman JA, Patick AK, Perros M, Scott AD, Whitby K, Wu H,
1001 Butler SL. 2010. HIV Capsid is a Tractable Target for Small Molecule Therapeutic Intervention.
1002 *PLoS Pathogens* **6**. doi:10.1371/journal.ppat.1001220

1003 Bunce CM, French PJ, Allen P, Mountford JC, Moor B, Greaves MF, Michell RH, Brown G. 1993.
1004 Comparison of the levels of inositol metabolites in transformed haemopoietic cells and their normal
1005 counterparts. *Biochem J* **289**:667–673. doi:10.1042/bj2890667

1006 Christensen DE, Ganser-Pornillos BK, Johnson JS, Pornillos O, Sundquist WI. 2020. Reconstitution
1007 and visualization of HIV-1 capsid-dependent replication and integration in vitro. *Sci New York N Y*
1008 **370**. doi:10.1126/science.abc8420

1009 Dick RA, Zadrozny KK, Xu C, Schur FKM, Lyddon TD, Ricana CL, Wagner JM, Perilla JR, Ganser-
1010 Pornillos BK, Johnson MC, Pornillos O, Vogt VM. 2018. Inositol phosphates are assembly co-
1011 factors for HIV-1. *Nature* **560**:1. doi:10.1038/s41586-018-0396-4

1012 Dickson CF, Hertel S, Ruan J, Ariotti N, Tuckwell A, Li N, Al-Izzi SC, Sierecki E, Gambin Y, Morris
1013 RG, Towers GJ, Böcking T, Jacques DA. 2023. Karyopherin mimicry explains how the HIV capsid
1014 penetrates nuclear pores. *bioRxiv* 2023.03.23.534032. doi:10.1101/2023.03.23.534032

1015 Dvory-Sobol H, Shaik N, Callebaut C, Rhee MS. 2022. Lenacapavir: a first-in-class HIV-1 capsid
1016 inhibitor. *Curr Opin Hiv Aids* **17**:15–21. doi:10.1097/coh.0000000000000713

1017 Fontana J, Keller PW, Urano E, Ablan SD, Steven AC, Freed EO. 2016. Identification of an HIV-1
1018 Mutation in Spacer Peptide 1 That Stabilizes the Immature CA-SP1 Lattice. *J Virol* **90**:972–978.
1019 doi:10.1128/jvi.02204-15

1020 Fricke T, Buffone C, Opp S, Valle-Casuso J, Diaz-Griffero F. 2014. BI-2 destabilizes HIV-1 cores
1021 during infection and Prevents Binding of CPSF6 to the HIV-1 Capsid. *Retrovirology* **11**:1–7.
1022 doi:10.1186/s12977-014-0120-x

1023 Ganser BK, Li S, Klishko VY, Finch JT, Sundquist WI. 1999. Assembly and analysis of conical models
1024 for the HIV-1 core. *Science (New York, NY)* **283**:80–3. doi:10.1126/science.283.5398.80

1025 Greig JA, Nguyen TA, Lee M, Holehouse AS, Posey AE, Pappu RV, Jedd G. 2020. Arginine-Enriched
1026 Mixed-Charge Domains Provide Cohesion for Nuclear Speckle Condensation. *Mol Cell* **77**:1237-
1027 1250.e4. doi:10.1016/j.molcel.2020.01.025

1028 Grime JM, Dama JF, Ganser-Pornillos BK, Woodward CL, Jensen GJ, Yeager M, Voth GA. 2016.
1029 Coarse-grained simulation reveals key features of HIV-1 capsid self-assembly. *Nature*
1030 *communications* **7**:11568. doi:10.1038/ncomms11568

1031 Gupta M, Pak AJ, Voth GA. 2022. Critical Mechanistic Role of Inositol Hexakisphosphate (IP6) in HIV-
1032 1 Viral Capsid Assembly. *Biorxiv* 2022.05.03.490470. doi:10.1101/2022.05.03.490470

1033 Highland CM, Tan A, Ricaña CL, Briggs JAG, Dick RA. 2023. Structural insights into HIV-1 polyanion-
1034 dependent capsid lattice formation revealed by single particle cryo-EM. *Proc National Acad Sci*
1035 **120**:e2220545120. doi:10.1073/pnas.2220545120

1036 Hotze EM, Le HM, Sieber JR, Bruxvoort C, McInerney MJ, Tweten RK. 2013. Identification and
1037 Characterization of the First Cholesterol-Dependent Cytolysins from Gram-Negative Bacteria.
1038 *Infect Immun* **81**:216–225. doi:10.1128/iai.00927-12

1039 Huang P-T, Summers BJ, Xu C, Perilla JR, Malikov V, Naghavi MH, Xiong Y. 2019. FEZ1 Is Recruited
1040 to a Conserved Cofactor Site on Capsid to Promote HIV-1 Trafficking. *Cell Reports*.
1041 doi:10.1016/j.celrep.2019.07.079

1042 Hulme AE, Kelley Z, Foley D, Hope TJ. 2015. Complementary Assays Reveal a Low Level of CA
1043 Associated with Viral Complexes in the Nuclei of HIV-1-Infected Cells. *Journal of virology*
1044 **89**:5350–61. doi:10.1128/jvi.00476-15

1045 Jacques DA, McEwan WA, Hilditch L, Price AJ, Towers GJ, James LC. 2016. HIV-1 uses dynamic
1046 capsid pores to import nucleotides and fuel encapsidated DNA synthesis. *Nature* **536**:349–53.
1047 doi:10.1038/nature19098

1048 Jennings J, Shi J, Varadarajan J, Jamieson PJ, Aiken C. 2020. The Host Cell Metabolite Inositol
1049 Hexakisphosphate Promotes Efficient Endogenous HIV-1 Reverse Transcription by Stabilizing the
1050 Viral Capsid. *Mbio* **11**. doi:10.1128/mbio.02820-20

1051 Kim K, Dauphin A, Komurlu S, McCauley SM, Yurkovetskiy L, Carbone C, Diehl WE, Strambio-De-
1052 Castillia C, Campbell EM, Luban J. 2019. Cyclophilin A protects HIV-1 from restriction by human
1053 TRIM5α. *Nat Microbiol* **4**:1–8. doi:10.1038/s41564-019-0592-5

1054 Kremer JR, Mastronarde DN, McIntosh JR. 1996. Computer Visualization of Three-Dimensional
1055 Image Data Using IMOD. *J Struct Biol* **116**:71–76. doi:10.1006/jsbi.1996.0013

1056 Lahaye X, Satoh T, Gentili M, Cerboni S, Conrad C, Hurbain I, Marjou AE, Lacabaratz C, Lelièvre J-
1057 DD, Manel N. 2013. The capsids of HIV-1 and HIV-2 determine immune detection of the viral
1058 cDNA by the innate sensor cGAS in dendritic cells. *Immunity* **39**:1132–42.
1059 doi:10.1016/j.immuni.2013.11.002

1060 Lamorte L, Titolo S, Lemke CT, Goudreau N, Mercier J-FF, Wardrop E, Shah VB, Schwedler UK von,
1061 Langelier C, Banik SS, Aiken C, Sundquist WI, Mason SW. 2013. Discovery of novel small-
1062 molecule HIV-1 replication inhibitors that stabilize capsid complexes. *Antimicrobial agents and*
1063 *chemotherapy* **57**:4622–31. doi:10.1128/aac.00985-13

1064 Letcher AJ, Schell MJ, Irvine RF. 2008. Do mammals make all their own inositol hexakisphosphate?
1065 *Biochem J* **416**:263–270. doi:10.1042/bj20081417

1066 Link JO, Rhee MS, Tse WC, Zheng J, Somoza JR, Rowe W, Begley R, Chiu A, Mulato A, Hansen D,
1067 Singer E, Tsai LK, Bam RA, Chou C-H, Canales E, Brizgys G, Zhang JR, Li J, Graupe M,

1068 Morganelli P, Liu Q, Wu Q, Halcomb RL, Saito RD, Schroeder SD, Lazerwith SE, Bondy S, Jin D,
1069 Hung M, Novikov N, Liu X, Villaseñor AG, Cannizzaro CE, Hu EY, Anderson RL, Appleby TC, Lu
1070 B, Mwangi J, Liclican A, Niedziela-Majka A, Papalia GA, Wong MH, Leavitt SA, Xu Y, Koditek D,
1071 Stepan GJ, Yu H, Pagratis N, Clancy S, Ahmadyar S, Cai TZ, Sellers S, Wolckenhauer SA, Ling J,
1072 Callebaut C, Margot N, Ram RR, Liu Y-P, Hyland R, Sinclair GI, Ruane PJ, Crofoot GE, McDonald
1073 CK, Brainard DM, Lad L, Swaminathan S, Sundquist WI, Sakowicz R, Chester AE, Lee WE, Daar
1074 ES, Yant SR, Cihlar T. 2020. Clinical targeting of HIV capsid protein with a long-acting small
1075 molecule. *Nature* **584**:1–5. doi:10.1038/s41586-020-2443-1

1076 Lu JM. 2020. Structural insights into HIV-1 capsid interactions by cryo-electron tomography.
1077 Cambridge University.

1078 Mallery DL, Kleinpeter AB, Renner N, Faysal KMR, Novikova M, Kiss L, Wilson MSC, Ahsan B, Ke Z,
1079 Briggs JAG, Saiardi A, Böcking T, Freed EO, James LC. 2021. A stable immature lattice packages
1080 IP6 for HIV capsid maturation. *Sci Adv* **7**:eabe4716. doi:10.1126/sciadv.abe4716

1081 Mallery DL, Márquez CL, McEwan WA, Dickson C, Jacques DA, Anandapadamanaban M, Bichel K,
1082 Towers GJ, Saiardi A, Böcking T, James LC. 2018. IP6 is an HIV pocket factor that prevents
1083 capsid collapse and promotes DNA synthesis. *eLife* **7**:e35335. doi:10.7554/elife.35335

1084 Márquez C, Lau D, Walsh J, Faysal KMR, Parker M, Turville S, Böcking T. 2019. Fluorescence
1085 Microscopy Assay to Measure HIV-1 Capsid Uncoating Kinetics in vitro. *Bio-protocol* **9**:e3297.
1086 doi:10.21769/bioprotoc.3297

1087 Márquez CL, Lau D, Walsh J, Shah V, McGuinness C, Wong A, Aggarwal A, Parker MW, Jacques
1088 DA, Turville S, Böcking T. 2018. Kinetics of HIV-1 capsid uncoating revealed by single-molecule
1089 analysis. *eLife* **7**. doi:10.7554/elife.34772

1090 Mastronarde DN. 2005. Automated electron microscope tomography using robust prediction of
1091 specimen movements. *J Struct Biol* **152**:36–51. doi:10.1016/j.jsb.2005.07.007

1092 Matreyek KA, Yücel SS, Li X, Engelman A. 2013. Nucleoporin NUP153 Phenylalanine-Glycine Motifs
1093 Engage a Common Binding Pocket within the HIV-1 Capsid Protein to Mediate Lentiviral
1094 Infectivity. *Plos Pathog* **9**:e1003693. doi:10.1371/journal.ppat.1003693

1095 Mattei S, Anders M, Konvalinka J, Kräusslich H-G, Briggs JA, Müller B. 2014. Induced maturation of
1096 human immunodeficiency virus. *J Virol* **88**:13722–31. doi:10.1128/jvi.02271-14

1097 Mattei S, Glass B, Hagen WJ, Kräusslich H-GG, Briggs JA. 2016. The structure and flexibility of
1098 conical HIV-1 capsids determined within intact virions. *Science (New York, NY)* **354**:1434–1437.
1099 doi:10.1126/science.aah4972

1100 Miles RJ, Kerridge C, Hilditch L, Monit C, Jacques DA, Towers GJ. 2020. MxB sensitivity of HIV-1 is
1101 determined by a highly variable and dynamic capsid surface. *Elife* **9**:e56910.
1102 doi:10.7554/elife.56910

1103 Müller TG, Zila V, Peters K, Schifferdecker S, Stanic M, Lucic B, Laketa V, Lusic M, Müller B,
1104 Kräusslich H-G. 2021. HIV-1 uncoating by release of viral cDNA from capsid-like structures in the
1105 nucleus of infected cells. *Elife* **10**:e64776. doi:10.7554/elife.64776

1106 Nicovich PR, Walsh J, Böcking T, Gaus K. 2017. NicoLase—An open-source diode laser combiner,
1107 fiber launch, and sequencing controller for fluorescence microscopy. *Plos One* **12**:e0173879.
1108 doi:10.1371/journal.pone.0173879

1109 Ning J, Zhong Z, Fischer DK, Harris G, Watkins SC, Ambrose Z, Zhang P. 2018. Truncated CPSF6
1110 Forms Higher-Order Complexes That Bind and Disrupt HIV-1 Capsid. *Journal of Virology*
1111 **92**:e00368-18. doi:10.1128/jvi.00368-18

1112 Obr M, Schur FKM, Dick RA. 2021. A Structural Perspective of the Role of IP6 in Immature and
1113 Mature Retroviral Assembly. *Viruses* **13**:1853. doi:10.3390/v13091853

1114 Patel PC, Beasley HK, Hinton A, Wanjalla CN. 2023. Lenacapavir (Sunlenca®) for the treatment of
1115 HIV-1. *Trends Pharmacol Sci* **44**:553–554. doi:10.1016/j.tips.2023.05.002

1116 Peng K, Muranyi W, Glass B, Laketa V, Yant SR, Tsai L, Cihlar T, Müller B, Kräusslich H-G. 2014.
1117 Quantitative microscopy of functional HIV post-entry complexes reveals association of replication
1118 with the viral capsid. *Elife* **3**:e04114. doi:10.7554/elife.04114

1119 Pornillos O, Ganser-Pornillos BK, Yeager M. 2011. Atomic-level modelling of the HIV capsid. *Nature*
1120 **469**:424–427. doi:10.1038/nature09640

1121 Price AJ, Fletcher AJ, Schaller T, Elliott T, Lee K, KewalRamani VN, Chin JW, Towers GJ, James LC.
1122 2012. CPSF6 defines a conserved capsid interface that modulates HIV-1 replication. *PLoS*
1123 *pathogens* **8**:e1002896. doi:10.1371/journal.ppat.1002896

1124 Price AJ, Jacques DA, McEwan WA, Fletcher AJ, Essig S, Chin JW, Halambage UD, Aiken C, James
1125 LC. 2014. Host Cofactors and Pharmacologic Ligands Share an Essential Interface in HIV-1
1126 Capsid That Is Lost upon Disassembly. *PLoS Pathogens* **10**:e1004459.
1127 doi:10.1371/journal.ppat.1004459

1128 Rankovic S, Ramalho R, Aiken C, Rousso I. 2018. PF74 reinforces the HIV-1 capsid to impair reverse
1129 transcription-induced uncoating. *Journal of Virology* JVI.00845-18. doi:10.1128/jvi.00845-18

1130 Rasaiyaah J, Tan CP, Fletcher AJ, Price AJ, Blondeau C, Hilditch L, Jacques DA, Selwood DL,
1131 James LC, Noursadeghi M, Towers GJ. 2013. HIV-1 evades innate immune recognition through
1132 specific cofactor recruitment. *Nature* **503**:402–405. doi:10.1038/nature12769

1133 Rebensburg SV, Wei G, Larue RC, Lindenberger J, Francis AC, Annamalai AS, Morrison J, Shkriabai
1134 N, Huang S-W, KewalRamani V, Poeschla EM, Melikyan GB, Kvaratskhelia M. 2021. Sec24C is
1135 an HIV-1 host dependency factor crucial for virus replication. *Nat Microbiol* 1–10.
1136 doi:10.1038/s41564-021-00868-1

1137 Renner N, Kleinpeter A, Mallery DL, Albecka A, Faysal KMR, Böcking T, Saiardi A, Freed EO, James
1138 LC. 2023. HIV-1 is dependent on its immature lattice to recruit IP6 for mature capsid assembly.
1139 *Nat Struct Mol Biol* 1–13. doi:10.1038/s41594-022-00887-4

1140 Renner N, Mallery DL, Faysal KMR, Peng W, Jacques DA, Böcking T, James LC. 2021. A lysine ring
1141 in HIV capsid pores coordinates IP6 to drive mature capsid assembly. *Plos Pathog* **17**:e1009164.
1142 doi:10.1371/journal.ppat.1009164

1143 Saito A, Ferhadian D, Sowd GA, Serrao E, Shi J, Halambage UD, Teng S, Soto J, Siddiqui MA,
1144 Engelman AN, Aiken C, Yamashita M. 2016. Roles of Capsid-Interacting Host Factors in
1145 Multimodal Inhibition of HIV-1 by PF74. *J Virol* **90**:5808–23. doi:10.1128/jvi.03116-15

1146 Santos CDS, Tartour K, Cimarelli A. 2016. A Novel Entry/Uncoating Assay Reveals the Presence of
1147 at Least Two Species of Viral Capsids During Synchronized HIV-1 Infection. *Plos Pathog*
1148 **12**:e1005897. doi:10.1371/journal.ppat.1005897

1149 Schaller T, Ocwieja KE, Rasaiyaah J, Price AJ, Brady TL, Roth SL, Hué S, Fletcher AJ, Lee K,
1150 KewalRamani VN, Noursadeghi M, Jenner RG, James LC, Bushman FD, Towers GJ. 2011. HIV-1
1151 Capsid-Cyclophilin Interactions Determine Nuclear Import Pathway, Integration Targeting and
1152 Replication Efficiency. *PLoS Pathogens* **7**:e1002439. doi:10.1371/journal.ppat.1002439

1153 Schirra RT, Santos NFB dos, Zadrozny KK, Kucharska I, Ganser-Pornillos BK, Pornillos O. 2023. A
1154 molecular switch modulates assembly and host factor binding of the HIV-1 capsid. *Nat Struct Mol*
1155 *Biol* 1–8. doi:10.1038/s41594-022-00913-5

1156 Selyutina A, Hu P, Miller S, Simons LM, Yu HJ, Hultquist JF, Lee K, KewalRamani VN, Diaz-Griffero
1157 F. 2022. GS-CA1 and lenacapavir stabilize the HIV-1 core and modulate the core interaction with
1158 cellular factors. *Iscience* **25**:103593. doi:10.1016/j.isci.2021.103593

1159 Shi J, Zhou J, Shah VB, Aiken C, Whitby K. 2011. Small-Molecule Inhibition of Human
1160 Immunodeficiency Virus Type 1 Infection by Virus Capsid Destabilization. *Journal of Virology*
1161 **85**:542–549. doi:10.1128/jvi.01406-10

1162 Sowd GA, Aiken C. 2021. Inositol phosphates promote HIV-1 assembly and maturation to facilitate
1163 viral spread in human CD4+ T cells. *Plos Pathog* **17**:e1009190. doi:10.1371/journal.ppat.1009190

1164 Sowd GA, Serrao E, Wang H, Wang W, Fadel HJ, Poeschla EM, Engelman AN. 2016. A critical role
1165 for alternative polyadenylation factor CPSF6 in targeting HIV-1 integration to transcriptionally
1166 active chromatin. *Proc National Acad Sci* **113**:E1054–E1063. doi:10.1073/pnas.1524213113

1167 Sowd GA, Shi J, Aiken C. 2021. HIV-1 CA inhibitors are antagonized by inositol phosphate
1168 stabilization of the viral capsid in cells. *J Virol* JVI0144521. doi:10.1128/jvi.01445-21

1169 Stacey JCV, Tan A, Lu JM, James LC, Dick RA, Briggs JAG. 2023. Two structural switches in HIV-1
1170 capsid regulate capsid curvature and host factor binding. *Proc National Acad Sci*
1171 **120**:e2220557120. doi:10.1073/pnas.2220557120

1172 Taylor WA. 2000. Change-point Analysis: a Powerful New Tool for Detecting Changes.

1173 Temple J, Tripler TN, Shen Q, Xiong Y. 2020. A snapshot of HIV-1 capsid–host interactions. *Curr Res*
1174 *Struct Biology* **2**:222–228. doi:10.1016/j.crstbi.2020.10.002

1175 Towers GJ, Hatziioannou T, Cowan S, Goff SP, Luban J, Bieniasz PD. 2003. Cyclophilin A modulates
1176 the sensitivity of HIV-1 to host restriction factors. *Nat Med* **9**:1138–1143. doi:10.1038/nm910

1177 Veiga N, Torres J, Domínguez S, Mederos A, Irvine RF, Díaz A, Kremer C. 2006. The behaviour of
1178 myo-inositol hexakisphosphate in the presence of magnesium(II) and calcium(II): Protein-free
1179 soluble InsP6 is limited to 49μM under cytosolic/nuclear conditions. *J Inorg Biochem* **100**:1800–
1180 1810. doi:10.1016/j.jinorgbio.2006.06.016

1181 Wei G, Iqbal N, Courouble VV, Francis AC, Singh PK, Hudait A, Annamalai AS, Bester S, Huang S-
1182 W, Shkriabai N, Briganti L, Haney R, KewalRamani VN, Voth GA, Engelman AN, Melikyan GB,
1183 Griffin PR, Asturias F, Kvaratskhelia M. 2022. Prion-like low complexity regions enable avid virus-
1184 host interactions during HIV-1 infection. *Nat Commun* **13**:5879. doi:10.1038/s41467-022-33662-6

1185 Yant SR, Mulato A, Hansen D, Tse WC, Niedziela-Majka A, Zhang JR, Stepan GJ, Jin D, Wong MH,
1186 Perreira JM, Singer E, Papalia GA, Hu EY, Zheng J, Lu B, Schroeder SD, Chou K, Ahmadyar S,
1187 Liclican A, Yu H, Novikov N, Paoli E, Gonik D, Ram RR, Hung M, McDougall WM, Brass AL,
1188 Sundquist WI, Cihlar T, Link JO. 2019. A highly potent long-acting small-molecule HIV-1 capsid
1189 inhibitor with efficacy in a humanized mouse model. *Nature Medicine* **25**. doi:10.1038/s41591-019-
1190 0560-x

1191 Zila V, Margiotta E, Turoňová B, Müller TG, Zimmerli CE, Mattei S, Allegretti M, Börner K, Rada J,
1192 Müller B, Lusic M, Kräusslich H-G, Beck M. 2021. Cone-shaped HIV-1 capsids are transported
1193 through intact nuclear pores. *Cell*. doi:10.1016/j.cell.2021.01.025

1194

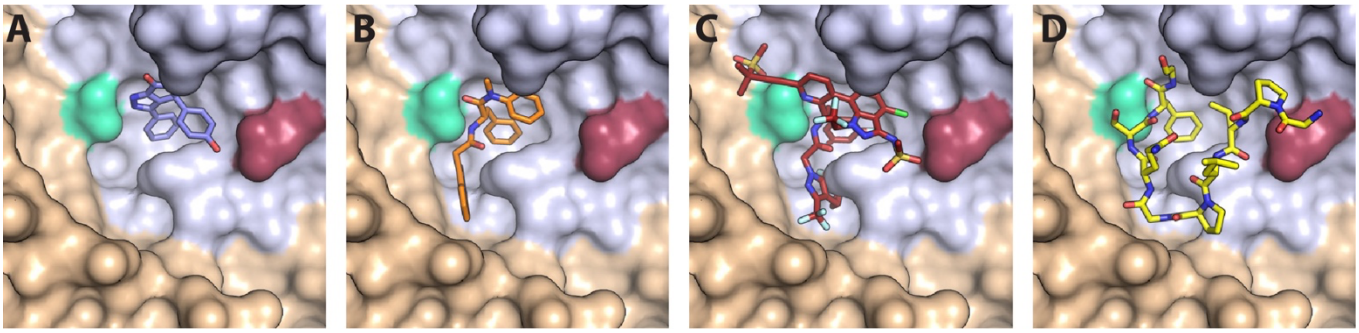

Figure 1. CA hexamer structures in complex with FG-binding pocket ligands. Two neighbouring CA molecules (grey, light brown) are shown as surface representation. Landmark residues N57 (pale green) and N74 (red-brown) are highlighted. Ligands are shown as sticks: **A.** BI-2. **B.** PF74. **C.** LEN. **D.** CPSF6 peptide. PDB IDs in A, B and D: 4U0F, 4U0E, 4U0A (Price et al., 2014). PDB ID in C: 6V2F (Link et al., 2020). Images were generated with PyMol version 2.3.5.

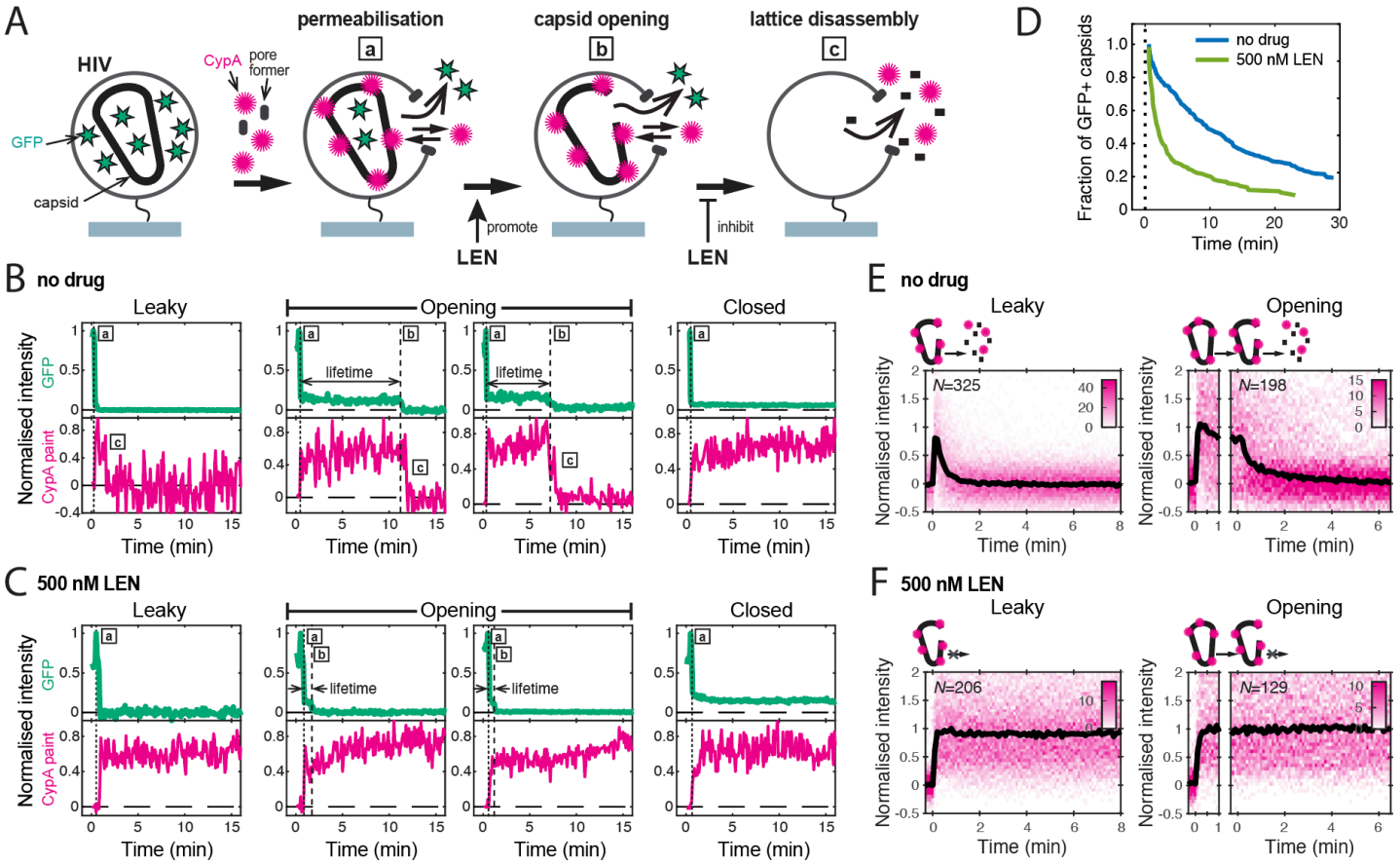

Figure 2. Single-particle HIV capsid uncoating kinetics measured by TIRF microscopy. A. Schematic diagram of a viral particle at different stages of uncoating detected in the assay. HIV particles were produced using a proviral construct with internal GFP that is released from the viral Gag protein during maturation and packaged as a solution phase marker inside the two compartments bound by the viral membrane and the capsid, respectively. These GFP-loaded HIV particles are immobilised on the coverslip surface and permeabilised in the presence of AF568-labelled CypA while recording fluorescence traces at the locations of individual HIV particles by TIRF microscopy. Permeabilisation of the viral membrane (step a) with a pore-forming protein leads to loss of ~80-90% of the GFP signal corresponding to the pool of GFP outside the capsid. AF568-CypA molecules diffuse through the membrane pores and bind to the capsid to reach a level that is proportional to the number of CA subunits in the capsid. Capsid opening (step b) leads to loss of the residual GFP that is inside the capsid. CA lattice disassembly (step c) is apparent from the rapid loss of the CypA paint signal. **B/C.** Example GFP release (blue-green) and CypA paint (magenta) traces for particles with capsids that are already leaky (i.e. contain defects and release all GFP in one step), undergo opening at various times after permeabilization or remain closed throughout the observation period. In the absence of drug (B), the CypA paint intensity decays rapidly when the capsid is no longer closed (complete loss of GFP signal). In the presence of 500 nM LEN (C), the CypA paint signal remains constant even when the GFP signal is completely lost showing that the drug stabilises the ruptured capsid. **D.** Analysis of the capsid lifetimes from all single-particle GFP release traces in the field of view to yield capsid survival curves (including “opening” and “closed”, excluding “leaky”). The faster decay in the presence of 500 nM LEN compared to no drug control shows that LEN induces rupture of the capsid. Data from a representative experiment (total number of traces): no drug (615); 500 nM LEN (281). **E/F.** Analysis of all single-particle CypA paint traces to yield heatmaps (magenta) and median traces (black line) of the CypA intensity measured at particles with leaky (left) or opening (right) capsids in the absence (E) or presence of 500 nM LEN (F). LEN prevents dissociation of CA from the lattice of capsids that are no longer closed cones. The number of HIV particles (*N*) for each condition is specified in the top left corner of the corresponding heatmap.

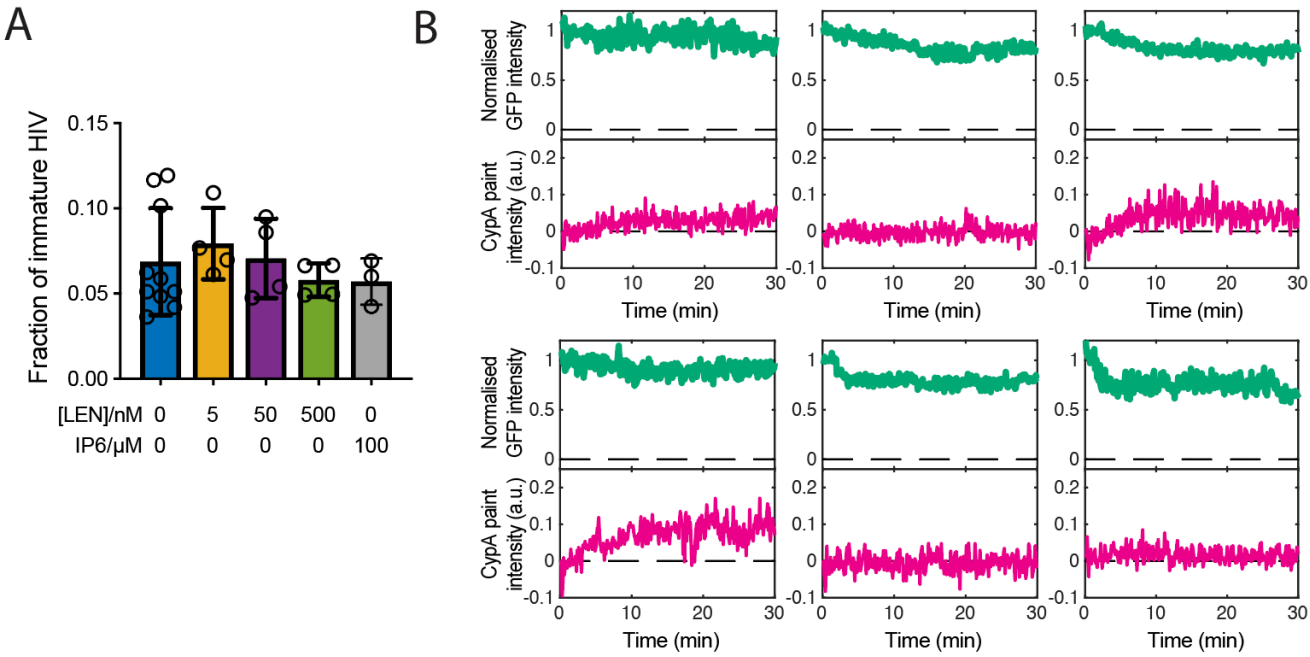

Figure 2–Figure Supplement 1. Maturation of HIV produced with Gag-iGFP. A. Bar chart showing the fraction of immature particles determined by TIRF imaging in the absence or presence of LEN or IP6. As expected, the fraction of immature particles does not depend on addition of LEN or IP6 during the uncoating experiment. **B.** Representative single-particle fluorescence traces characteristic of an immature Gag lattice. Unlike particles that have undergone proteolysis, immature particles release little or no GFP because it remains part of the Gag polyprotein anchored to the inside of the viral membrane. CypA binding to these particles is negligible or slow because the CypA loops are poorly accessible in the context of the immature Gag lattice. Particles identified as immature on the basis of these criteria are excluded from analysis since they do not contain a mature capsid.

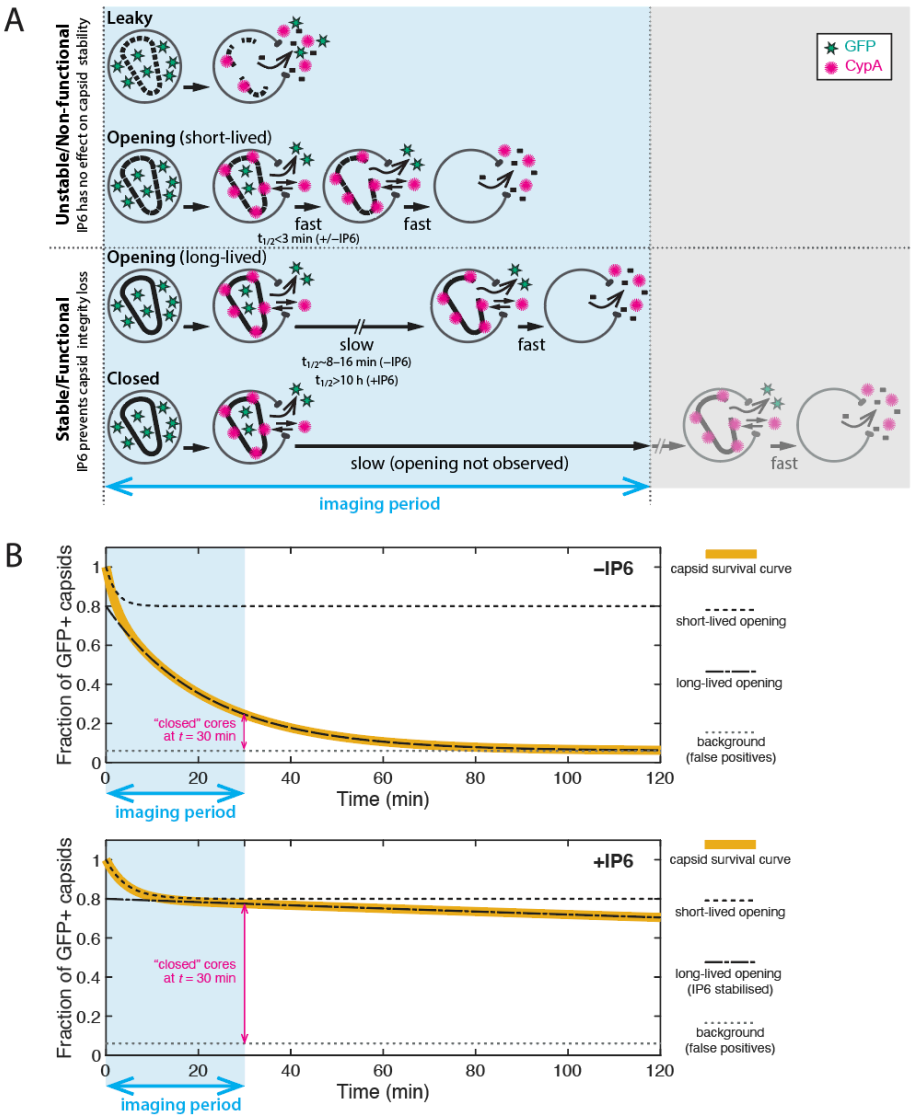

Figure 2–Figure Supplement 2. Interpretation of TIRF uncoating data and limitations of the assay. A. Cartoon showing the different uncoating phenotypes observed in the dual colour (iGFP release and CypA paint) TIRF uncoating assay. Two broad stability types can be distinguished: (1) Unstable/non-functional capsids. "Leaky" (total GFP release upon virion permeabilization) and "opening–short-lived" capsids (half-life of 1–2 min) are intrinsically unstable and cannot be rescued by IP6. These capsids are presumably incompletely or improperly assembled and non-functional. (2) Stable/functional capsids. The subpopulation of "opening–long-lived" capsids (half-life of 8–16 min) can be stabilised by IP6, which keeps the closed cone intact by preventing loss of the first subunit(s), greatly increasing the half-life. Capsids that remain closed at the end of the experiment are presumed to have the same uncoating behaviour (i.e. are structurally and functionally the same) as "opening–long-lived" capsids, whereby the imaging period was simply not long enough to observe the opening of all capsids in the field of view. *Limitations of the TIRF uncoating assay:* As with all imaging methodologies, the particle detection limit depends on factors that influence the signal-to-noise ratio (e.g. laser power, exposure time, penetration depth, imaging frequency, photophysical properties of the fluorophore). *Known artefacts of iGFP:* (1) Particles produced with iGFP have a broad distribution of GFP intensities, and dim particles with closed capsids that contain too little GFP can fall below the detection limit and thus appear as GFP-negative/CypA paint-positive spots. (2) A small proportion of GFP-positive spots persists throughout the experiment and remains negative for CypA paint. We attribute this background of false positives (typically <5% of the preparation, see also panel B) to particles containing residual uncleaved Gag-iGFP. *Known artefacts of CypA paint:* The efficiency of using CypA paint analysis to detect leaky capsids depends on the imaging frequency. This is because the CypA paint signal of leaky capsids is too short-lived (often appearing in only one frame or missed entirely when imaged at a low frequency) to be detected in a noisy baseline. For example, ~20% of leaky capsids that are detected by GFP release are also detected by CypA paint at an imaging frequency of 1 frame every 6 s. **B.** Idealised capsid survival curves in the absence (top) and presence (bottom) of IP6. Leaky particles are excluded from survival analysis. The survival curve (yellow line) is a convolution of the decay curves corresponding to the short- (dashed black line) and long-lived (dash-dotted black line) subpopulations. Only the long-lived subpopulation responds to IP6. The survival curves decays to a background level above zero (dotted grey line) that is presumably due to false positive signals. Parameter values used for calculating the traces: (A) Fractions of short-lived/long-lived/background particles are 20%/74%/6%, respectively. The half-lifes are $t_{1/2}^{short} = 1.5$ min and $t_{1/2}^{long} = 15$ min, (B) as for A but $t_{1/2}^{short} = 3$ min and $t_{1/2}^{long} = 10$ h.

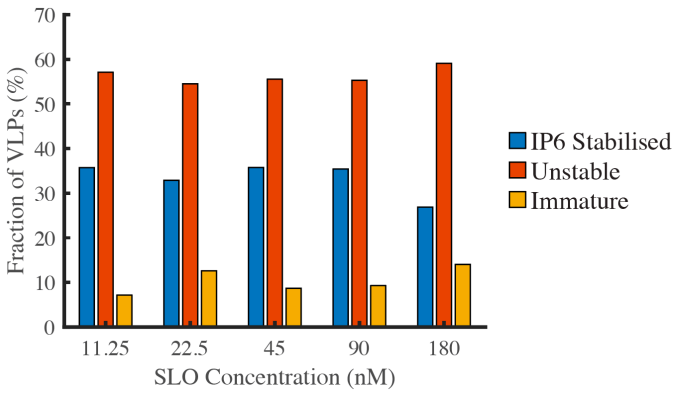

Figure 2–Figure Supplement 3. The pore-forming protein SLO does not affect capsid stability. GFP-loaded HIV particles produced with Gag-iGFP were captured onto the surface of a glass coverslip and imaged by TIRF microscopy while flowing a solution containing the pore-forming protein SLO (to permeabilise the viral membrane) and IP6 (to prevent uncoating of stable capsids). The fractions of particles with IP6-stabilised capsids (retaining a low intensity signal corresponding to encapsidated GFP), particles with unstable capsids (complete loss of GFP intensity) and immature particles (high intensity signal due to unprocessed Gag-iGFP) was independent of the SLO concentration between 11.25 and 180 nM.

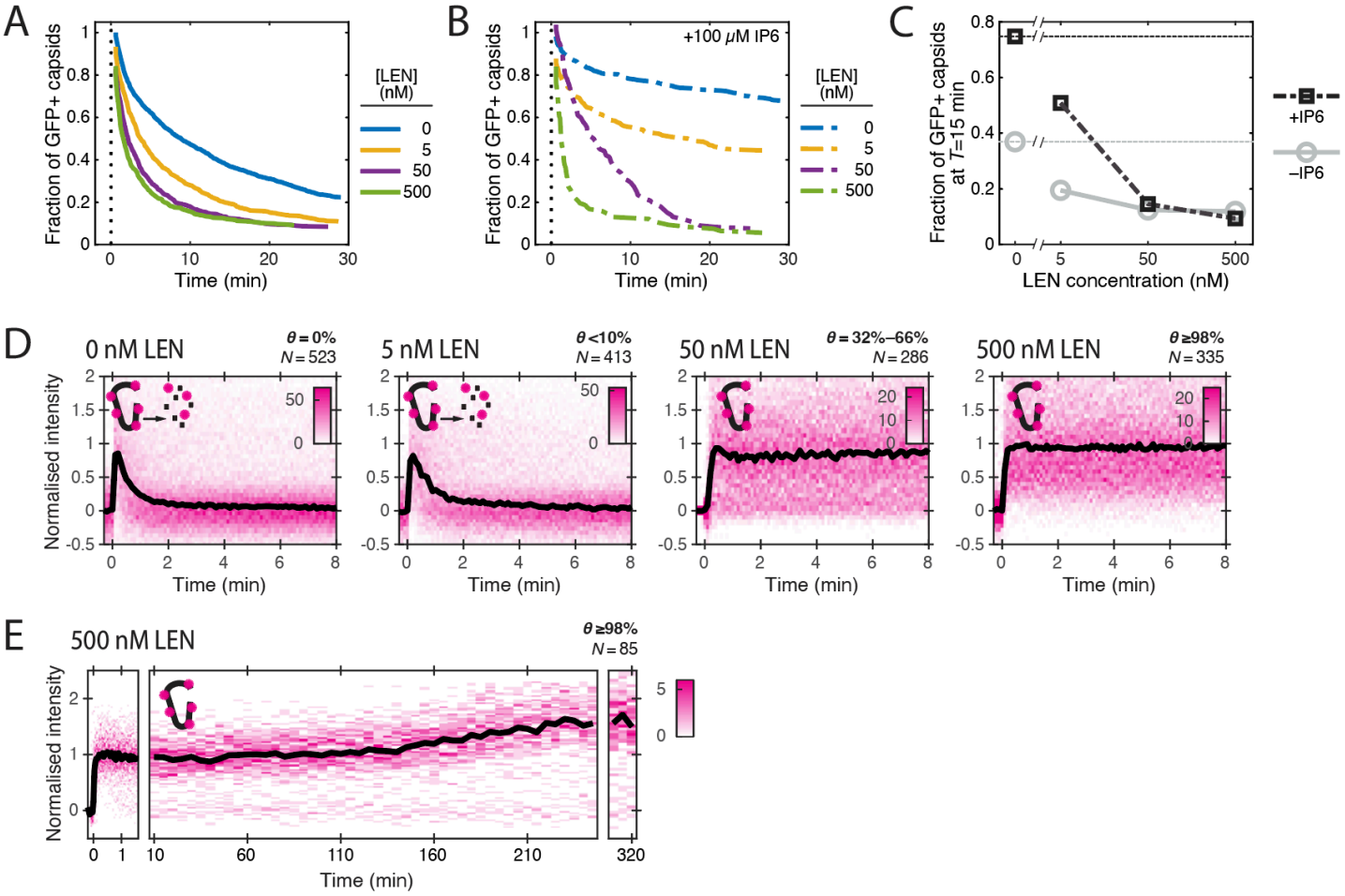

Figure 3. LEN accelerates capsid opening and subsequently promotes CA lattice stability. Single-particle analysis of the effect of 0–500 nM LEN −/+100 μM IP6 on capsid uncoating via GFP release and CypA paint. **A.** Capsid survival curves showing that the drug induces rupture of the capsid. Pooled data from multiple experiments (total number of traces/number of experiments): 0 nM (4325/10); 0.5 nM (1242/4); 5 nM (1585/4); 50 nM (1520/5); 500 nM (1048/4). **B.** Capsid survival curves showing that IP6 inhibits capsid opening in the absence of LEN and partially counteracts the drug-induced rupture of the capsid at low but not high concentrations of LEN. Pooled data from multiple experiments (total number of traces/number of experiments): 0 nM LEN+IP6 (836/3); 5 nM LEN+IP6 (589/2); 50 nM LEN+IP6 (321/1); 500 nM LEN+IP6 (238/1). **C.** Fraction of closed (GFP-positive) capsids at t = 15 minutes of the uncoating experiments shown in A and B. **D.** Heatmaps (magenta) and median traces (black line) of the CypA intensity measured at particles with leaky or opening capsids in the presence of 0–500 nM LEN showing that LEN stabilises the CA lattice of ruptured capsids above an occupancy (θ) threshold of ~30–66%. The occupancy at the time of membrane permeabilization was calculated as described in Figure 4–Figure Supplement 1. **E.** Heatmap (magenta) and median trace (black line) of the CypA intensity of particles (leaky/opening) showing that 500 nM LEN prevents CA loss from the ruptured capsid for at least 5 hours. The number of HIV particles (N) for each condition in D and E is specified above the corresponding heatmap.

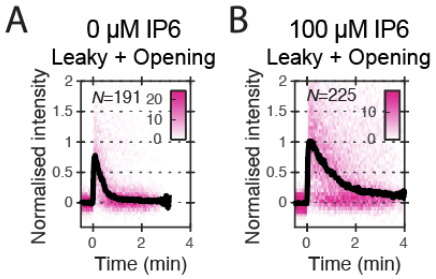

Figure 3–Figure Supplement 1. Heatmaps (magenta) and median traces (black line) of the CypA intensity measured at particles with leaky or opening capsids in the absence (A) or presence (B) of 100 μM IP6. The number of HIV particles (*N*) for each condition is specified in the top left corner of the corresponding heatmap.

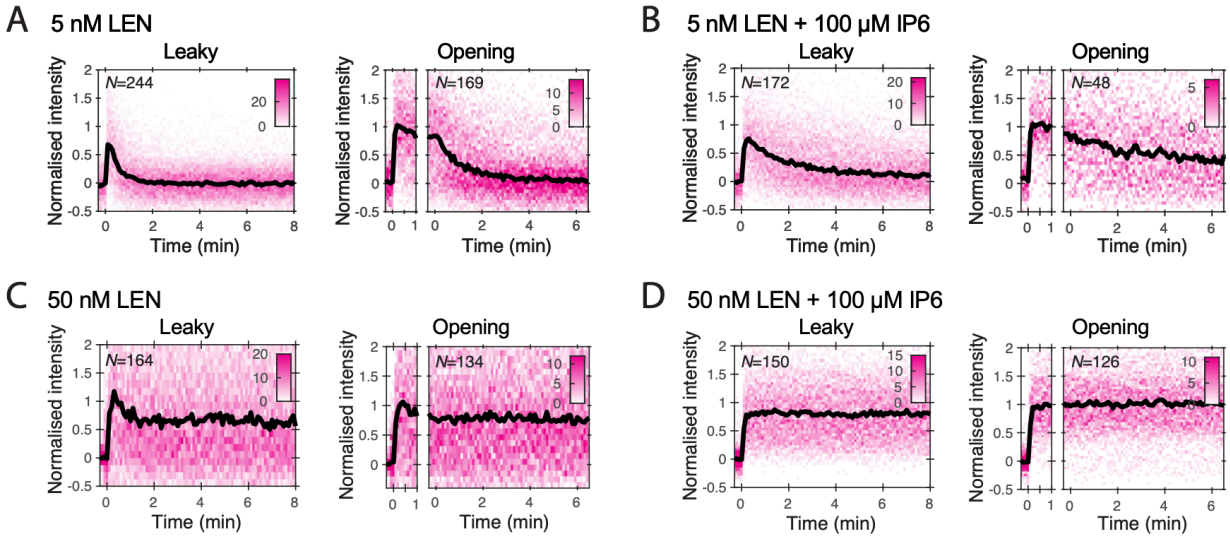

Figure 3–Figure Supplement 2. Heatmaps (magenta) and median traces (black line) of the CypA intensity measured at particles with leaky (left) or opening (right) capsids. **A/B.** 5 nM LEN in the absence (A) or presence (B) of 100 μM IP6. The presence of IP6 slows capsid disassembly in the presence of 5 nM LEN but does not prevent it. **C/D.** 50 nM LEN in the absence (C) or presence (D) of 100 μM IP6. 50 nM LEN stabilises the CypA paint signal, regardless of whether IP6 is present. The number of HIV particles (*N*) for each condition is specified in the top left corner of the corresponding heatmap.

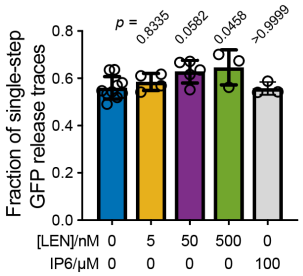

Figure 3–Figure Supplement 3. Effect of LEN on the fraction of particles that release their total GFP content in a single step. Single-step GFP release traces in the absence of LEN are attributed to “leaky” capsids that cannot retain GFP upon membrane permeabilization. This leaky fraction is 56±5% for virions analysed in Figures 2 and 3. Addition of LEN during the uncoating experiment causes a concentration-dependent increase in the fraction of single-step GFP release traces (amounting to a an icrease by 9% to 65±5% at 500 nM LEN), which we attribute to rapid LEN-induced rupture of intact capsids (too fast to be resolved as a separate step in the uncoating traces recorded with a frame rate of 1 frame every 6 s). As expected, IP6 does not affect the “leaky” fraction because IP6 stabilises closed cones but is unable to prevent disassembly of CA lattices with open edges. Statistical comparisons using one-way ANOVA with Dunnett’s multiple comparison test. The *p* values of the comparison between control (0 nM LEN) and different LEN concentrations are given above the corresponding bars.

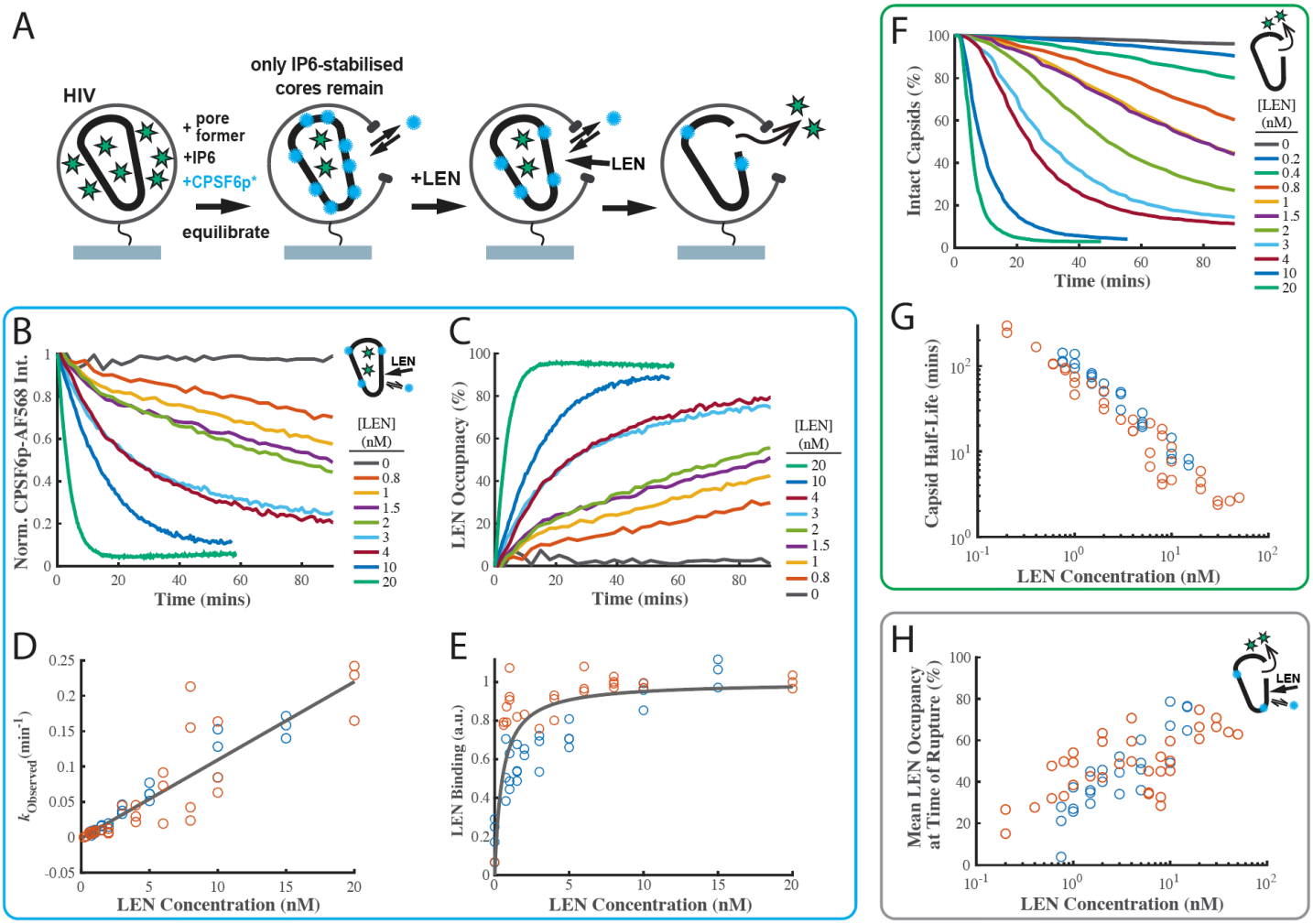

Figure 4. LEN binding to capsids is slow at concentrations close to the EC95 and limits the kinetics of LEN-induced capsid rupture. A. Schematic diagram of the TIRF microscopy competition binding and capsid opening assay. GFP-loaded HIV attached to the glass coverslip are permeabilised using SLO and incubated in a solution 30 µM IP6. During this period, unstable capsids that do not respond to IP6 fall apart. Labelled CPSF6p (0.2 nM) functions as a paint probe (occupying ~2% of free FG binding pockets at equilibrium). LEN displaces CPSF6p-AF568 on the capsid over time, leading to a decrease of the labelled CPSF6p intensity. Rupture of the capsid is detected by GFP release. **B-E.** Analysis of CPSF6p-AF568 signal disappearance to extract LEN binding kinetics and affinity. (B) Mean CPSF6p-AF568 displacement curves measured at all IP6-stabilised capsids in the field of views on the presence of 0–20 nM LEN. (C) LEN binding curves calculated from the CPSF6p-AF568 displacement curves in B. (D) Observed LEN binding rates (obtained from an exponential fit of the binding curves) as a function of LEN concentration. The slope of the linear fit to data from two experiments provides a LEN binding rate of k_{on} = 1.84±0.78 × 10^5 M^{-1} s^{-1}. **E.** Equilibrium binding curve for LEN on IP6-stabilised capsids. The fit (grey line) of an equilibrium binding model to the combined combined data from two experiments provided the dissociation constant of K_D = 0.51±0.58 nM. **F-G.** Analysis of GFP release to determine the effect of LEN on capsid integrity. (F) Survival curves of IP6-stabilised capsids in the presence of 0–20 nM LEN. (G) Half life of the intact capsid as a function of LEN concentration determined from the curves in F as the time point where half of the capsids had released GFP. **H.** Combined analysis of the GFP release and CPSF6p-AFMean LEN occupancy levels at the time of capsid rupture as a function of LEN concentration. Orange and blue circles in D, E, G and H correspond to two sets of experiments conducted with different viral preparations, different fluorophores, and different preincubation condition. Experiments shown as orange circles used CPSF6p-Alexa Fluor 568, which was added to the capsid at the same time as LEN. Experiments shown as blue circles used CPSF6p-ATTO643, which was preincubated with HIV prior to LEN exposure. The CPSF6p displacement and capsid opening curves for the data set for the blue circles are shown in Figure 4–Figure Supplement 3.

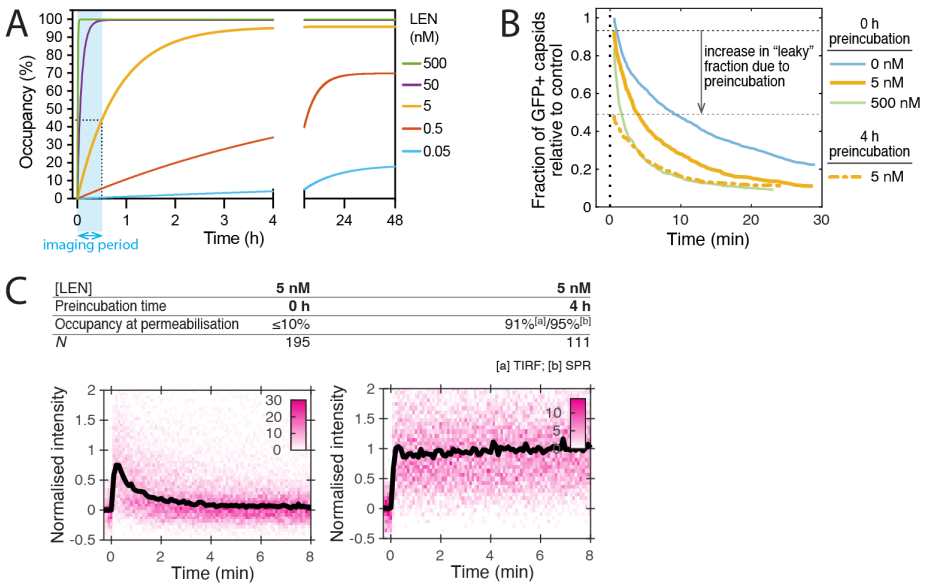

Figure 4–Figure Supplement 1. A. Predicted occupancy of binding pockets on the CA lattice with LEN as a function of time ($\theta(t)$) for different LEN concentrations. The occupancy is defined as the fraction of FG binding pockets on the capsid that are occupied with a LEN molecule and was calculated using the following equation: $\theta(t) = \theta_{eq}(1\text{-}\exp(\text{-}(k_{on}\times c_{LEN} + k_{off}) \times t)$, where θ_{eq} is the occupancy at equilibrium, c_{LEN} is the LEN concentration, k_{on} is the association rate constant and k_{off} is the dissociation rate constant. The curves were calculated using published values of k_{on} = 6.5E4 $M^{-1}s^{-1}$ and k_{off} = 1.4E-5 s^{-1} determined by surface plasmon resonance spectroscopy (Link et al., 2020). **B/C.** Single-particle analysis of capsid uncoating in the presence of 5 nM LEN added to the viral particles at the start (0 h preincubation) or 4 h before the start (4 h preincubation) of the TIRF assay. (B) Capsid survival curves show that preincubation with drug increases capsid rupture. Pooled data from multiple experiments (total number of traces/number of experiments): 5 nM LEN with 4 h preincubation (1159/3). Traces without preincubation (0/5/500 nM) are replotted from Figure 3A for comparison. (C) CypA paint heatmaps and median CypA paint intensity traces of leaky and opening capsids show that preincubation is required to stabilise the CA lattice after capsid rupture. The occupancy at the time of permeabilization (2 minutes) was calculated as above using the published rate constants determined by surface plasmon resonance spectroscopy or TIRF microscopy (this work). The number of HIV particles (*N*) for each condition is specified above the corresponding heatmap.

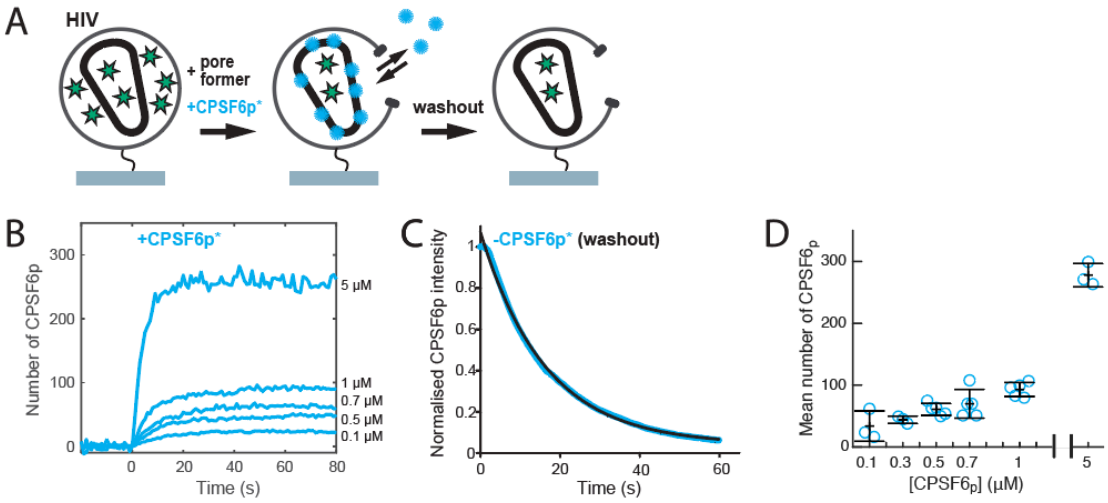

Figure 4–Figure Supplement 2. Binding of CPSF6 peptide to closed capsids. A. Schematic of the binding assay. **B.** Mean binding traces recorded at the indicated concentrations of labelled CPSF6 peptide. Binding traces were recorded at the locations of viral particles with closed capsid, whereby t = 0 corresponds to the time of viral membrane permeabilization. **C.** Mean CPSF6 peptide intensity measured at closed capsids after wash-out of CPSF6 peptide from the flow channel at t = 0. The black line represents a fit of the data with a single exponential decay function. **D.** Mean number of labelled CPSF6 peptides bound per capsid determined from binding experiments (see panel B for an example). Each symbol represents an independent binding experiment, black bars indicate mean and standard deviation.

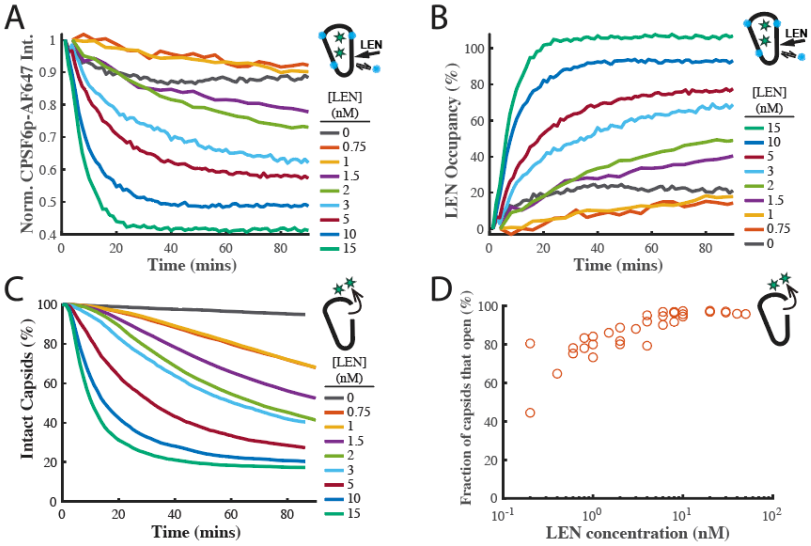

Figure 4–Figure Supplement 3. A. Mean CPSF6p-Atto643 displacement curves measured at all IP6-stabilised capsids in the field of views in the presence of 0–15 nM LEN. The Atto643 label resulted in a higher background than observed for the AF568 label in Figure 4. **B.** LEN binding curves calculated from the CPSF6p-Atto643 displacement curves in A. **C.** Survival curves of IP6-stabilised capsids in the presence of 0–15 nM LEN. **D.** Fraction of IP6-stabilised capsids that open in the presence of 0.2–50 nM LEN. The LEN-induced caspsid rupture efficiency drops to below 65% at concentration ≤0.4 nM LEN.

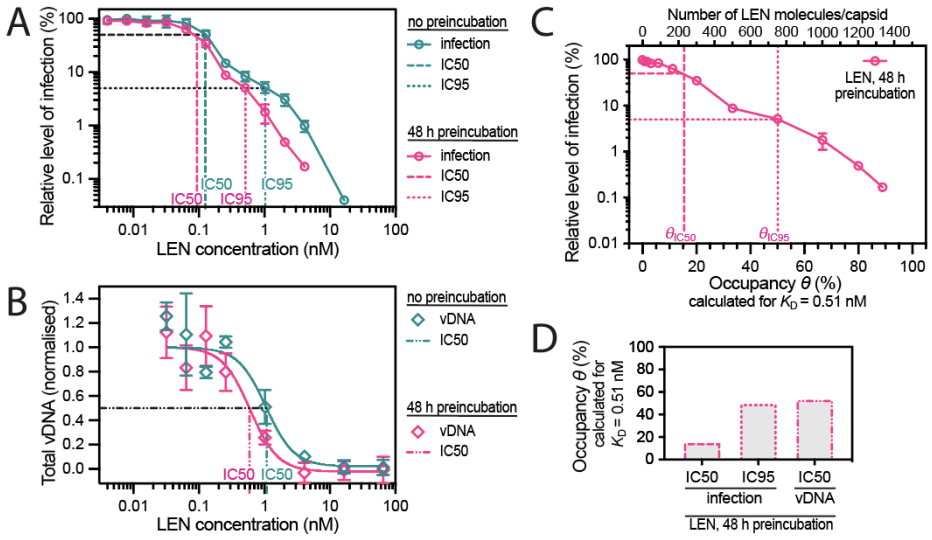

Figure 5. Preincubating HIV particles with LEN is required to obtain the full effect of the drug on capsid stability, HIV infection and reverse transcription. A. Dose-response curves of Jurkat cells infected with VSV-G-pseudotyped GFP-encoding virus that was preincubated for 0 h or 48 h with the corresponding concentration of LEN. The number of infected cells was determined by flow cytometry 48 h post infection. Data points represent percent infectivity relative to the vehicle control. The graph shows data from four (0 h preincubation) or three (48 h preincubation) independent experiments. The vertical dashed lines indicate the IC50 values determined from least squares fits of the curves and the vertical dotted lines indicate the IC95 values determined as the concentration where the relative level of infection reaches 5% (0 h preincubation: 1.024 nM [5.3% infection]; 48 h preincubation: 0.512 nM [5.1% infection]). **B.** Quantification using qPCR of total viral DNA from Jurkat cells collected 24 h after infection with VSV-G-pseudotyped GFP-encoding virus as in panel D (with 0 h or 48 h preincubation with LEN). Normalized copy numbers (mean ± SD) from two independent experiments with two technical repeats each. Least squares fit (solid line) providing IC50 values of ~1080 pM without preincubation and ~590 pM with 48 h preincubation. **C.** Relative infection after 48 h preincubation of HIV with varying LEN concentrations (same data as in A) plotted as a function of occupancy (θ) of the FG binding pockets on the capsid. **D.** Bar charts of occupancy at the IC50 and IC95 for infection and at the IC50 for vDNA synthesis. The occupancy in C and D was calculated for each LEN concentration assuming a dissociation constant (K_D) of 0.51 nM using the equation $\theta_{eq} = c_{LEN} / (c_{LEN} + K_D)$, where θ_{eq} is the occupancy at equilibrium and c_{LEN} is the LEN concentration.

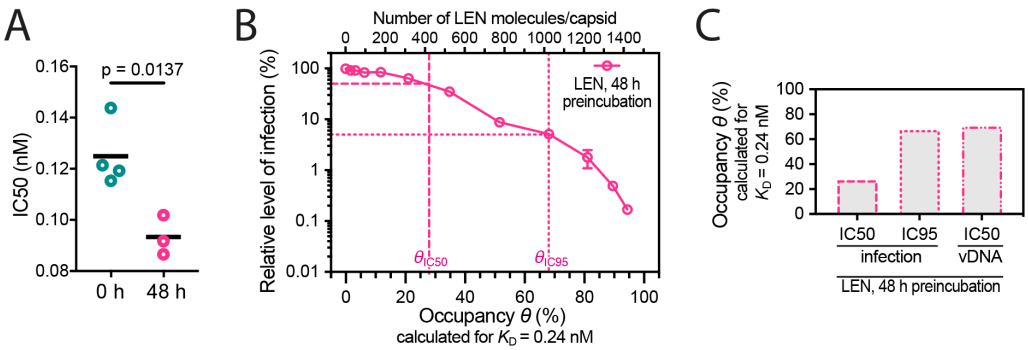

Figure 5–Figure Supplement 1. A. Relative IC50 values determined from least squares fits of the data in Figure 5A giving values of 125±13 pM without preincubation and 93±8 pM with 48 h preincubation. Statistical analysis using an unpaired two-tailed t-test. **B/C.** Same plots as in Figure 5C and D but assuming the dissociation constant (K_D) of 0.24 nM determined by surface plasmon resonance spectroscopy (Link et al., 2020). (B) Relative infection after 48 h preincubation of HIV with varying LEN concentrations plotted as a function of occupancy (θ) of the FG binding pockets on the capsid. (C) Bar charts of occupancy at the IC50 and IC95 for infection and at the IC50 for vDNA synthesis.

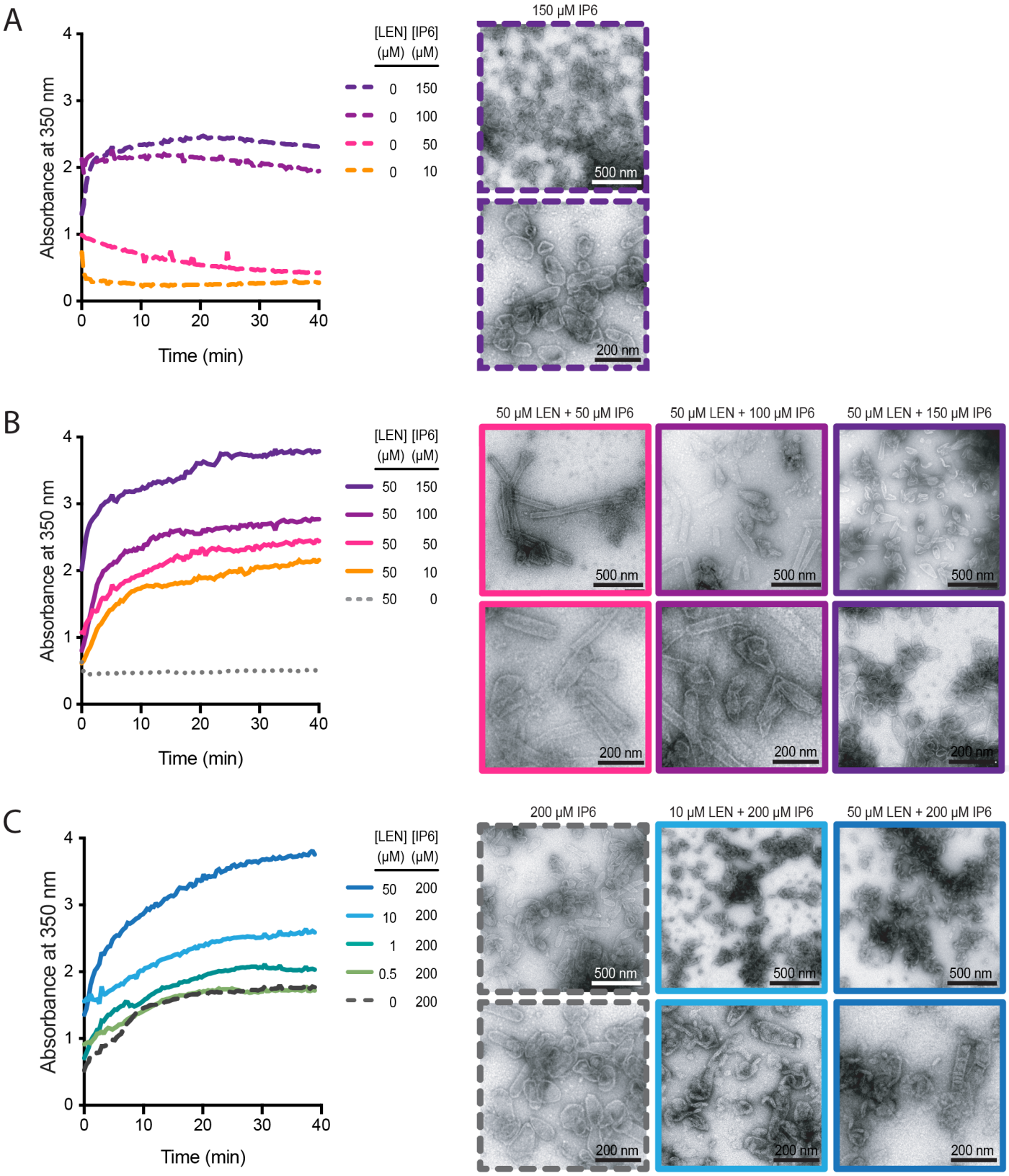

Figure 6. IP6 and LEN synergise to promote CA assembly. In vitro assembly reactions of CA (75 μM) were carried out in 50 mM MES (pH 6.0) containing 1 mM DTT and monitored in real time by absorbance measurements at 350 nm. The assembly products obtained at the end of the reaction were imaged by negative staining electron microscopy. **A/B.** Assembly kinetics (left) and products (right) formed at 10–150 μM in the absence (A) or the presence (B) of 50 μM LEN. **C.** Assembly kinetics (left) and products (right) formed at 0–50 μM LEN in the presence of 200 μM IP6.

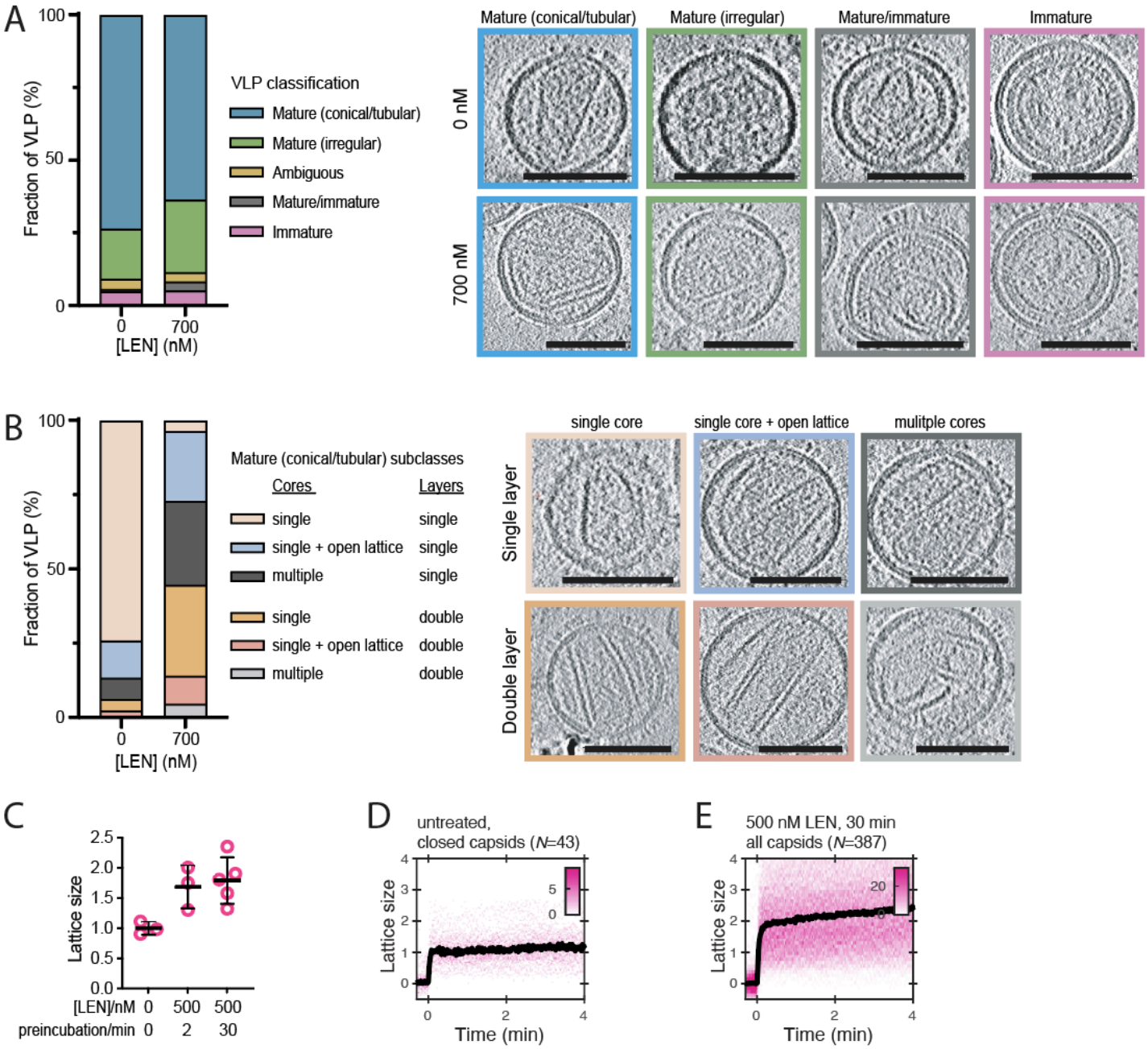

Figure 6–Figure Supplement 1. LEN promotes assembly of additional CA structures outside the capsid in mature HIV particles. A/B. CryoET analysis of untreated HIV and HIV incubated with 700 nM LEN for 30 min. A total of 139 untreated and 96 drug-treated viral particles were analysed, and the frequency of each phenotype is plotted as a percentage in the bar plots. Slices through representative tomograms of each phenotype are shown. Scale bars, 100 nm. (A) Virions were classified as either immature, mature/immature, ambiguous, mature (irregular) or mature (conical/tubular). (B) The mature (conical/tubular) particles from C were further divided into subclasses reflecting the number of CA assemblies and the absence or presence of assemblies with two CA layers. **C.** CypA paint intensity analysis to estimate the level of CA lattice assembly ("lattice size") in HIV particles preincubated with 500 nM LEN for 30 min before permeabilization relative to the lattice size of closed capsids in untreated HIV particles. Comparison of lattice size in untreated control (3 experiments) and HIV preincubated with 500 nM LEN for 2 minutes (3 experiments) or 30 minutes (5 experiments) showing that drug induces an increase in lattice size. Example CypA paint heatmaps are shown panels D and E. **D/E.** CypA paint intensity analysis to estimate the level of CA lattice assembly ("lattice size") in HIV particles preincubated with 500 nM LEN for 30 min before permeabilization relative to the lattice size of closed capsids in untreated HIV particles. Example CypA paint heatmaps (magenta) and median traces (black) of closed capsids in untreated HIV (D) and all capsids in HIV preincubated with drug (E). The number of HIV particles (*N*) for each condition is specified above the corresponding heatmap.

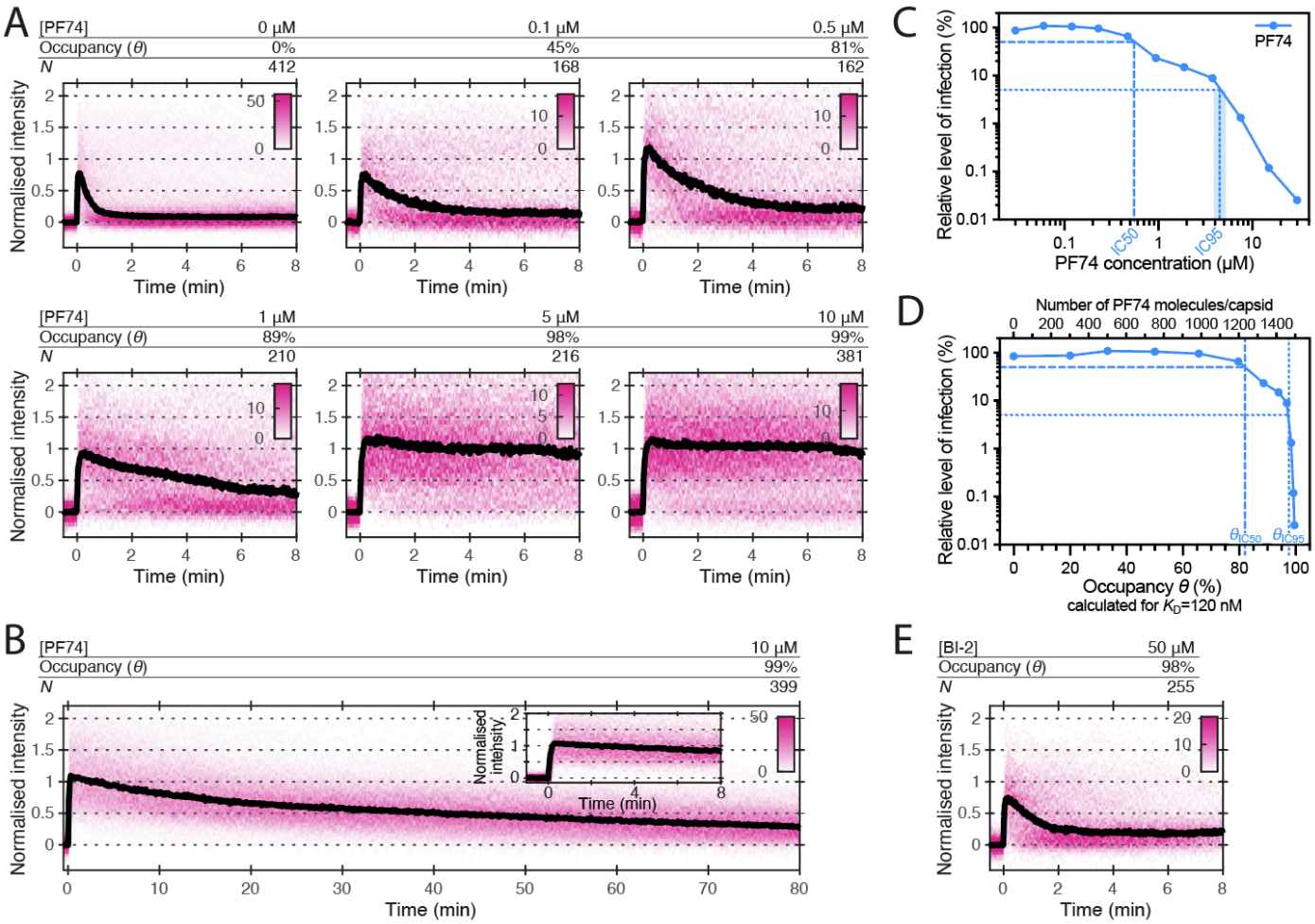

Figure 7. Effects of PF74 and BI-2 on CA lattice stability. A/B. Heatmaps (magenta) and median traces (black line) of the CypA intensity measured at particles with leaky or opening capsids in the presence of 0–10 μM PF74 showing that PF74 stabilises the CA lattice at concentrations ≥5 μM. (A) PF74 titration in 8 min experiments. (B) 10 μM PF74 in an 80 min experiment showing that capsid lattices disassemble over this time period. The inset shows the first 8 min of the trace. **C.** Dose-response curve of Jurkat cells infected with VSV-G-pseudotyped GFP-encoding virus in the presence of the indicated concentrations of PF74. The number of infected cells was determined by flow cytometry 48 h post infection. Data points represent percent infectivity relative to the vehicle control. The dashed line indicates the IC50 determined from least squares fits of the curve (~0.6 μM, corresponding to ~5×K_D). The dotted line indicates the IC95 (4–5 μM, corresponding to 30–40×K_D). **D.** Relative infection (same data as in C) plotted as a function of occupancy (θ) of the FG binding pockets on the capsid calculated for each PF74 concentration assuming a K_D of 120 nM. **E.** Heatmap (magenta) and median trace (black line) of the CypA intensity at particles with leaky or opening capsids in the presence of 50 μM BI-2 showing that BI-2 does not stabilise the CA lattice.

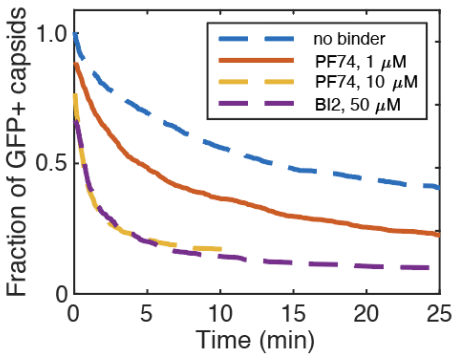

Figure 7 – Figure Supplement 1. PF74 and BI-2 binding at high occupancy leads to capsid rupture. Capsid survival curves were determined from GFP release traces. The control curve (no binder) and the curves determined in the presence of 10 uM PF74 and 50 uM BI-2 are reproduced from Marquez et al, 2018.

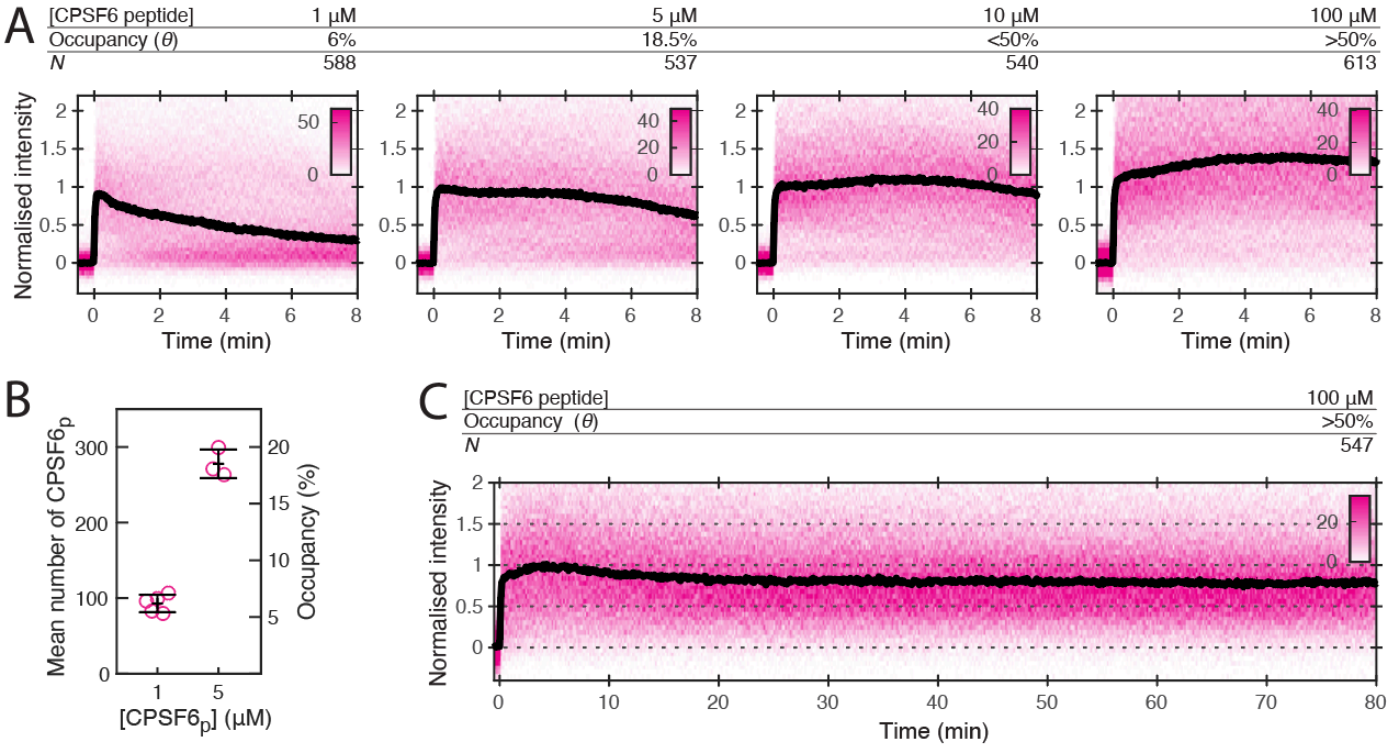

Figure 8. CPSF6 peptide stabilises the CA lattice at low occupancy. A. Heatmaps (magenta) and median traces (black line) of the CypA intensity measured at particles with leaky capsids in the presence of 1–100 µM CPSF6 peptide showing that the peptide stabilises the CA lattice at concentrations below the K_D of the peptide-CA hexamer interaction. The occupancy (θ) at 1 µM and 5 µM was determined experimentally (see B) while θ was estimated for higher concentratrions assuming a K_D of 50 µM. **B.** Mean number of CPSF6 peptides bounds per capsid determined from CPSF6p-Cys-AF568 binding experiments. Each symbol represents an independent binding experiment, black bars indicate mean and standard deviation. **C.** Heatmap (magenta) and median trace (black line) of the CypA intensity at particles with leaky or opening capsids in the presence of 100 µM CPSF6 monitored over 80 minutes, showing long-term stabilisation of the CA lattice.

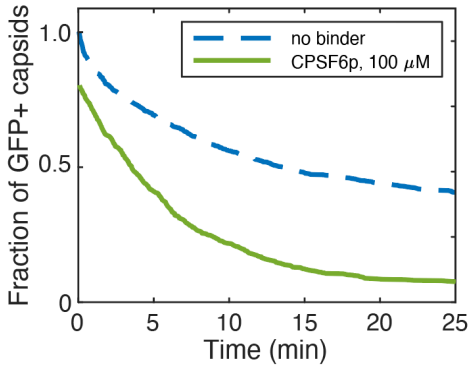

Figure 8 – Figure Supplement 1. Capsid survival curves were determined from GFP release traces. The control curve (no binder) is reproduced from Marquez et al, 2018.

Link JO, Rhee MS, Tse WC, Zheng J, Somoza JR, Rowe W, Begley R, Chiu A, Mulato A, Hansen D, Singer E, Tsai LK, Bam RA, Chou C-H, Canales E, Brizgys G, Zhang JR, Li J, Graupe M, Morganelli P, Liu Q, Wu Q, Halcomb RL, Saito RD, Schroeder SD, Lazerwith SE, Bondy S, Jin D, Hung M, Novikov N, Liu X, Villaseñor AG, Cannizzaro CE, Hu EY, Anderson RL, Appleby TC, Lu B, Mwangi J, Liclican A, Niedziela-Majka A, Papalia GA, Wong MH, Leavitt SA, Xu Y, Koditek D, Stepan GJ, Yu H, Pagratis N, Clancy S, Ahmadyar S, Cai TZ, Sellers S, Wolckenhauer SA, Ling J, Callebaut C, Margot N, Ram RR, Liu Y-P, Hyland R, Sinclair GI, Ruane PJ, Crofoot GE, McDonald CK, Brainard DM, Lad L, Swaminathan S, Sundquist WI, Sakowicz R, Chester AE, Lee WE, Daar ES, Yant SR, Cihlar T. 2020. Clinical targeting of HIV capsid protein with a long-acting small molecule. *Nature* 584:1–5. doi:10.1038/s41586-020-2443-1

Price AJ, Jacques DA, McEwan WA, Fletcher AJ, Essig S, Chin JW, Halambage UD, Aiken C, James LC. 2014. Host Cofactors and Pharmacologic Ligands Share an Essential Interface in HIV-1 Capsid That Is Lost upon Disassembly. *PLoS Pathogens* 10:e1004459. doi:10.1371/journal.ppat.1004459